8-4-2022

Impacts of Spatial Resolution and Viewing Angle on Remotely Sensed Estimates of Spartina alterniflora Aboveground Biomass

Avery Miller
axm9863@rit.edu

Recommended Citation

Miller, Avery, "Impacts of Spatial Resolution and Viewing Angle on Remotely Sensed Estimates of Spartina alterniflora Aboveground Biomass" (2022). Thesis. Rochester Institute of Technology. Accessed from

RIT

Impacts of Spatial Resolution and Viewing Angle on Remotely Sensed Estimates of *Spartina alterniflora* Aboveground Biomass

by

Avery Miller

A Thesis Submitted in Fulfillment of the Requirements for the Degree of Master of Science in Environmental Science

Program in Environmental Science
Thomas H. Gosnell School of Life Sciences

Rochester Institute of Technology
Rochester, NY
4 August, 2022

Committee Approval

Anna Christina Tyler, PhD Date

Chair of Committee, Thesis Advisor

Charles M. Bachmann, PhD Date

Committee Member

Jan van Aardt, PhD Date

Committee Member

Table of Contents

Acknowledgements:

I express my gratitude to my advisor Dr. Christy Tyler for her consistent support throughout my graduate work, and for pushing me to continue on at RIT after my undergraduate degree - I have learned so much in these last few years, and can't imagine a better way to spend that time. I would like to acknowledge Dr. Jan van Aardt and Dr. Karl Korfmacher for introducing me to the fascinating fields of remote sensing and large scale geospatial analysis, which have held my interest and been my passion for years now. I would also like to acknowledge Dr. Charles "Chip" Bachmann for his guidance and assistance in the technical aspects of this research, and for all of the knowledge he has been able to impart to me along the way.

I would like to thank all of my family and friends for the constant support and encouragement these last few years - it is greatly appreciated. For being patient and putting up with my questions as a coding novice, I would like to thank my friends Ka Chan and Nathan Warms for their help with all things Python related. Additionally, I would like to thank everyone involved in the 2019 field campaigns: Christy Tyler, Chip Bachmann, David Osgood, Tim Bauch, Chris Lapszynski, Sydney VanWinkle, Sarah Ponte, Wendy Owens, Cora Ann-Johnston, and Evan Squier. Without their help, this project would not have been possible.

Finally, I'm grateful for the support given to this project by the National Geographic Explorers program under Grant NGS-382R-18, for the support provided by NSF DEB Grants #1237733 and #1832221 (VCR-LTER), and for funding from the College of Science and the Thomas H. Gosnell School of Life Sciences at the Rochester Institute of Technology.

List of Tables and Figures

Abstract:

Coastal salt marshes sequester large quantities of “blue carbon” in plant biomass and sediments, and provide numerous other valuable ecosystem functions and services. However, these ecosystems are increasingly threatened by external stressors, including rising sea levels and a changing climate, which have resulted in large losses of tidal marsh habitat. Measuring plant biomass is critical for understanding how carbon storage may be affected as stressors continue to cause marsh losses, and for improving conservation and management efforts. A number of studies have quantified aboveground biomass (AGB) in salt marshes using remote sensing techniques, and with the development of high resolution sensors there is excellent potential to improve estimates over large scales. However, few studies have evaluated how variability in spatial resolution and viewing angle across platforms impacts AGB estimates, despite the large range of potential imaging systems available. Using 3 cm and 6 cm resolution nadir hyperspectral drone imagery, and 0.5-3 cm oblique imagery collected from a ground-based camera at three viewing angles from two different-aged barrier island salt marshes in Virginia, USA, I evaluated the accuracy of regression models predicting *S. alterniflora* AGB from vegetation indices across resolution and viewing angle. The overall best performing linear regression models were obtained using the 3 cm nadir drone imagery. However, the best 6 cm regression models demonstrated only minor losses in accuracy relative to 3 cm. AGB estimates from obliquely angled imagery were less accurate than either nadir resolution. The most accurate oblique models were obtained at the highest viewing angle, with performance decreasing as the viewing angle became shallower. These results suggest that not all platforms perform similarly

within salt marsh ecosystems, and that both spatial resolution and viewing angle must be considered in choice of imaging systems.

Introduction:

Salt marshes provide a number of valuable ecosystem functions and services to both human society and to the environment (Costanza et al. 1997). Commonly found along shorelines and barrier islands, these ecosystems protect coastal areas from storms and erosion, cycle nutrients, and provide habitat for unique species, with some recent estimates valuing salt marshes at almost $241,000 per hectare per year (Costanza et al. 1997, Costanza et al. 2014, Nelleman et al. 2009). Current salt marsh extent is estimated to be approximately 5.5 M ha worldwide, much of which can be found along the eastern and Gulf coasts of North America (Mcowen et al. 2017).

In addition to the ecosystem functions and services discussed above, salt marshes are among the most productive ecosystems on Earth, sequestering significant quantities of "blue carbon" in sediments and plant biomass, making them valuable for abating climate change (Chastain et al. 2018, Duarte et al. 2005, McLeod et al. 2011, McTigue et al. 2020, Nelleman et al. 2009). Along the Atlantic coast of North America, large quantities of plant biomass are contained within dense monocultures of *Spartina alterniflora* (marsh cordgrass), which dominate the intertidal zone. Importantly, *S. alterniflora* phenotypic expression is controlled by elevation: tall-form grows at low elevations along creek banks and open water, while short-form *S. alterniflora* grows at higher elevations at the interface with the high marsh (Valiela et al. 1978). Due to the heterogeneity in elevation and other drivers present within these ecosystems, high variability in above-ground biomass (AGB), and in turn, carbon storage, can be observed across the intertidal zone (Richards et al. 2005). However, salt marsh ecosystems are threatened by rising sea levels, climate change, die-off events, and other anthropogenic stressors, with significant habitat losses being observed both worldwide and within Virginia's barrier islands (Bertness et al. 2002, Bridgham et al. 2006, Donnelly & Bertness 2001, Deaton et al. 2017, Gedan et al. 2009, Kearney & Grace 1988, Kirwan et al. 2009, Minchinton et al. 2002, Tiner et al. 2002). Considering the quantity of carbon stored within salt marshes, increasing our understanding of the spatial distribution of AGB within these ecosystems is necessary to inform conservation efforts and understand the potential reduction in carbon storage potential.

Considering the heterogeneity present in most salt marshes, it can be challenging to adequately capture this variation with field sampling alone. Remote sensing techniques have been used extensively to scale from plot level studies to landscape level estimates of AGB in salt marshes, freshwater wetlands, and seagrass meadows (Armstrong 1993, Doughty & Cavanaugh 2019, Miller et al. 2019, O'Donnell et al. 2016, Rendong et al. 2004, Schalles et al. 2013, Wang et al. 2017). These studies and others have used regression modeling to correlate AGB measurements taken from field sampling plots to the intensity of specific wavelengths or vegetation indices (VI) at the pixel(s) intersecting with the plot. Typically, models produced using this method are linear or multiple regression models using a single vegetation index or combination of indices as predictors of AGB, with the resulting model then being extrapolated to every pixel within the region of interest (Miller et al. 2019, O'Donnell et al. 2016, Rendong et al. 2004). Often generated using imagery collected at nadir, these models generally result in a good fit between predicted and measured AGB values; using multiple regression, Wang et al. (2017) found a combination of VIs resulting in a model predicting *S. alterniflora* AGB in coastal China with an R^2 of 0.704 using 0.78 m hyperspectral imagery. Similarly, O'Donnell et al. (2016) used single linear regression to create a model predicting *S. alterniflora* AGB in Georgian (US) salt marshes with an R^2 of 0.70 using 1 m hyperspectral imagery.

Often used in the past, the wide coverage and temporal consistency of coarse-resolution platforms - such as airborne and satellite sensors - makes them valuable for observing ecosystems on a large scale and monitoring changes over time. However, the heterogeneity present within salt marshes often occurs on scales smaller than the pixel sizes of these sensors (McLeod et al. 2011, Pennings et al. 2005). On a larger scale, ecological and edaphic characteristics vary depending on marsh age (Goldsmith 2019, He et al. 2016, Morgan & Short 2002, Osgood & Zieman 1993, Tyler et al. 2003, Walsh 1998), while AGB and *S. alterniflora* phenology vary widely over the course of the growing season (Ellison et al. 1986), making widespread assessment over time important for fully understanding marsh productivity. The development of UAS imaging allows for the collection of centimeter scale data that may capture this heterogeneity more accurately, when compared to airborne and satellite platforms. While less frequently used, the collection of off-nadir imagery may be more beneficial than nadir imaging for remote sensing of *S. alterniflora* erectophile canopies, by capturing the broad sides of the culm while reducing the amount of background sediment visible.

Given the variety of spatial resolutions and viewing angles achievable with current platforms and sensors - and that have been previously used in the literature to generate these large-scale estimates of AGB - it is important to understand if and how these different imaging techniques affect remotely sensed estimates of AGB. In this regard, one past study noted discrepancies in *S. alterniflora* AGB estimates when using data of varying spatial resolutions within an inverted PROSAIL model, where average AGB retrieved from across a number of salt marsh scenes changed inconsistently as the imagery was increasingly downsampled (Eon et al. 2019). While Eon et al. (2019) used centimeter-scale hyperspectral imagery acquired at oblique viewing geometries, this same effect was potentially observed by O'Donnell et al. (2016), where resampling their 1 m resolution *S. alterniflora* AGB regression model for use with 30 m Landsat imagery decreased model performance from an R^2 of 0.70 to an R^2 of 0.51. While a wide array of imaging platforms providing various spatial resolutions and viewing angles have been used in the literature independently for AGB modeling, no direct comparisons have been made to evaluate any differences in their relative accuracies for the same scenes at a single point in time.

Using contemporaneously collected drone and obliquely angled mast-mounted imagery, this study aims to (1) quantify differences in remotely sensed estimates of *S. alterniflora* AGB among the varying spatial resolutions and viewing angles these platforms provide, (2) evaluate differences among estimates generated using various VI regression models, and (3) examine applicability of models across the growing season. Given the common use of regression modeling in the literature to predict AGB using a variety of sensors and platforms, it is critical to understand how performance varies under different imaging parameters. In doing so, this study aims to understand which spatial resolutions and viewing angles yield the most accurate regression models of AGB, to enable more informed decision making when choosing between the various platforms and sensors used for contemporary remote sensing applications.

Methods:

Site Selection:

Located approximately six miles off the eastern coast of the Delmarva Peninsula in Virginia, Hog Island features back-barrier salt marshes, sandy beaches, dunes, and upland areas. As part of the Virginia Coast Reserve Long-Term Ecological Research (VCR LTER) site, Hog Island is an ideal environment to study salt marsh ecosystems given its undeveloped, isolated nature and consistent data record. Additionally, the southern portion of the island features a salt marsh chronosequence, where the age of the marsh varies over short spatial scales, depending on the recency of the last major overwash event and *S. alterniflora* recolonization. This chronosequence includes marshes ranging in age from over 150 yr old to five yr old at the time of this study, allowing for the observation of a wide variety of conditions.

Two chronosequence sites were selected for study in 2019: the pre-1870 Mature Marsh site ("Broadwater"), and the 1989/2011 Young Marsh site (Figure 1). Adjacent to a tidal creek, the Mature Marsh site is populated entirely by *S. alterniflora*. This site features fine-grained sediments rich in organic matter, with an approximately 50% silt fraction and a significantly lower sand content than the other marshes in the chronosequence (Goldsmith 2020). The Young Marsh consists of a mosaic of marshes that range in age from roughly 8 to approximately 33 yr. These ages correspond to establishment dates between 2011 and 1989, based on the first appearance in aerial imagery of *S. alterniflora* on the sediment platform. This site features greater variability in elevation, resulting in the presence of both *S. alterniflora* monocultures and high marsh species, including *Salicornia virginica, Limonium carolinianum,* and *Distichlis* *spicata*. Since its establishment, this marsh expanded both seaward and landward, and additional overwash events have been observed. Additionally, the Young Marsh features sediments with a nearly 80% sand fraction, and significantly lower OM (2-3%) than the Mature Marsh (Goldsmith 2019). Both sites are tidally inundated, with average elevations of a few centimeters below mean sea level.

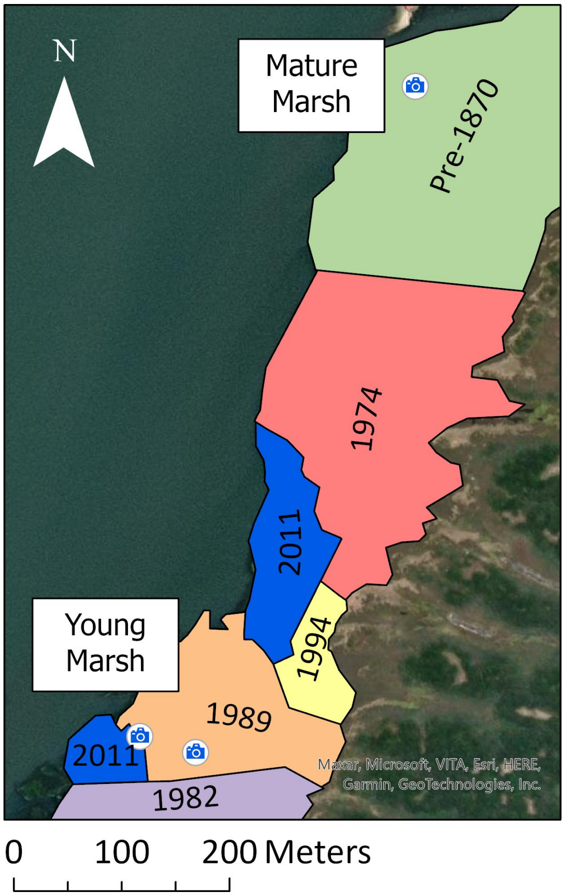

Figure 1 (right): Locations of the Mature Marsh and Young Marsh sites imaged in 2019.

Establishment of Imaging Scenes and Ground-Truth Plots:

Nine scenes within the Mature Marsh and Young Marsh sites were selected for imaging in 2019 using the mast-mounted hyperspectral system (Bachmann et al. 2019). Twelve ground-truth plots were established within each scene, for a total of 48 plots at the Mature Marsh site and 60 plots at the Young Marsh site (Figure 2). Plots were distributed approximately randomly throughout each scene to capture spatial heterogeneity and to provide data at varying distances from the oblique viewing geometry of the mast-mounted imaging system. Each 0.5 m by 0.5 m plot was marked using PVC poles and brightly colored stake flags to mark the corners of each plot to ensure their visibility within the imagery. This plot size is small enough to provide a focused view of ecological conditions at a point, but large enough to include >100 pixels at the typical ground-sampling distances (GSD) of the mast-mounted and drone imaging platforms. Coordinates and elevation at each corner of the ground-truth plots was collected using a Trimble R10 RTK GNSS system, which provides sub-centimeter horizontal accuracy and 15 mm vertical accuracy (Trimble Geospatial).

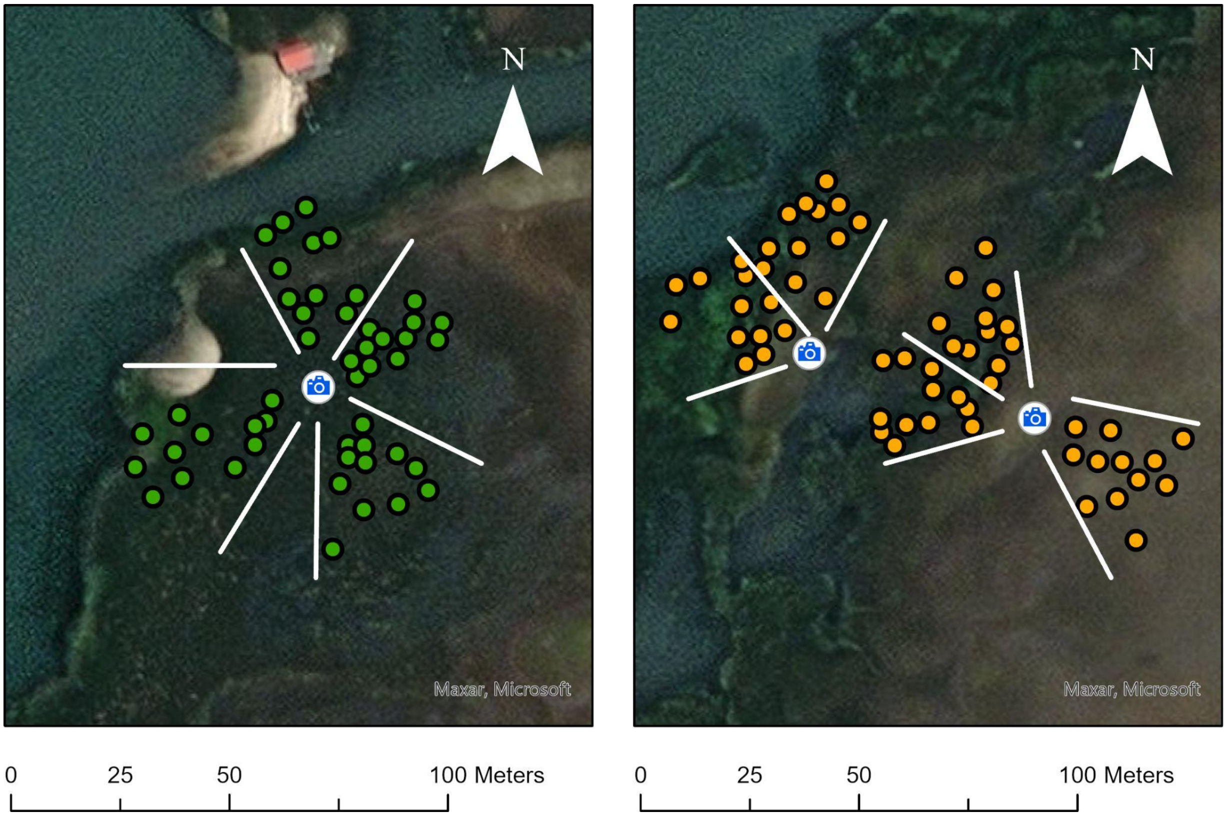

Figure 2: Imaging scenes and ground-truth plots established for 2019 data collection at the Mature Marsh (left) and Young Marsh sites (right).

Imaging of Marsh Sites:

Hyperspectral imagery of the Mature Marsh and Young Marsh study sites acquired at oblique viewing geometries was collected on July 25 and 26, 2019, respectively, prior to collection of validation and site characterization data, which occurred on the same days. Additional imagery of the Young Marsh site was collected on October 7, 2019 from the same camera positions, to allow for interseasonal comparisons of *S. alterniflora* AGB. Before imaging, two calibrated, near-Lambertian Spectralon reflectance targets were placed within each scene and marked with GPS. Imagery was collected using a Headwall VNIR Micro-Hyperspec High Efficiency E-series system, a pushbroom sensor with 1600 across-track pixels, that took measurements in 371 spectral bands between 400 nm and 1000 nm. The view orientation of this system ranges from -34° to 34° in pitch, and -175° to 175° in yaw, since the system is mounted within a General Dynamics Vector-20 maritime-rated pan-tilt unit (General Dynamics, Bachmann et al. 2019). Using a BlueSky AL-3 Lift Series telescopic mast, five heights above the sediment surface were imaged at each scene: 2, 4, and 6 meters (AL-3 2020). Imagery was collected using a 4 ms exposure time, a viewing zenith angle from 0° to -34°, and five azimuth angles (in the majority of cases) to encompass the approximately 60° wide scenes: -30°, -15°, 0°, 15°, and 30°. Although the mast positions and scenes imaged were not exactly the same as in previous years, the 2019 imagery continued the yearly data record of the Mature Marsh and Young Marsh sites established in 2017 (Eon et al. 2019). All imagery recorded from oblique viewing geometries was converted from raw digital numbers to radiance using a calibration performed with a Labsphere Helios 20 integrating sphere (Bachmann et al. 2019), before converting to reflectance using the Spectralon reference panels placed within each imaging scene.

Hyperspectral drone imagery of both sites was also collected in July 2019 during the field campaign. Imagery of the Mature Marsh and Young Marsh sites was collected at 50 m and 100 m altitudes using a Matrice 600 pro drone outfitted with the MX1 payload, including a Headwall nano Hyperspec, a Tamarisk 640 LWIR, a Velodyne VLP-16 LiDAR, and Mako G-419 RGB camera. At these elevations, the Headwall nano Hyperspec system was able to achieve approximately 3 cm and 6 cm GSD, respectively. This payload collected visible-NIR hyperspectral, LiDAR, broadband thermal, and high-resolution multispectral data, with SWIR hyperspectral imagery being collected during separate flights. All drone imagery was then orthorectified and converted to reflectance using the three-point empirical line method prior to analysis.

Sediment Characterization:

At each ground-truth plot, 10 one cm deep sediment cores were collected in July 2019 using a 1.1 cm diameter syringe corer. Five cores were pooled together to create two samples, both of which were analyzed for bulk density (BD) and moisture content (at time of sampling), by taking the mass before and after drying at 60 °C for 24-48 hrs. One pooled sample from each plot was analyzed for sediment organic matter (SOM) content using the mass loss on ignition technique: after taking the wet mass, the sample was heated to 550 °C for four hr, after which the mass was taken again. The other sample from each plot was homogenized using a mortar and pestle, and analyzed for carbon and nitrogen content using a Perkin Elmer 2400 Elemental Analyzer.

Total phosphorus at 1 cm was analyzed by adding 0.5 ml of 50% w/v $Mg(NO_3)_2$ to 0.1 g of dried, homogenized sediment, before heating each sample to 550 °C for 90 min. After, 10 ml of 1N HCl was added to each sample and vortexed, before placing each sample on a roto-shaker for 16 hr. Samples were diluted by a factor of 10 before allowing for color development, before measuring their absorbance at 827 nm. Absorbance values were compared to those of standard phosphate solutions (Aspila et al. 1976, Murphy & Riley 1962).

Additionally, one 10 cm deep sediment core was collected from each ground-truth plot in July 2019, which was also analyzed for BD and moisture content. After, each sample was homogenized and divided for further analysis, using the same methods as above for organic matter, carbon, nitrogen, and phosphorus content.

Porewater salinity was measured by inserting a perforated sampling probe to a depth of 10 cm in the sediment at each ground-truth plot, withdrawing up to 5 ml of porewater (Berg & McGlathery 2001) and measuring salinity using an automatic temperature compensating refractometer.

Benthic Chlorophyll *a* Quantification:

Two 1 cm deep soil cores were collected with a 1.1 cm diameter syringe corer and placed within 15 ml test tubes at each ground-truth plot sampled during the July and October field campaigns. Each core was wrapped in foil and placed on ice, until it could be frozen at -80 °C. Chlorophyll *a* and phaeopigment concentrations were then quantified according to the methods proposed by Jeffrey & Humphrey (1975). Six ml of cold 90% acetone was added to each soil core, before shaking to resuspend the sediment. Each sample was then sonicated for one minute three times, with one minute rest intervals in between. The samples were then placed in a -20 °C freezer overnight to allow for chlorophyll extraction to occur. After extraction, samples were resuspended and centrifuged for 5 min. at 2,500 rpm. Using a Shimadzu 1800 dual beam spectrophotometer, absorbance at 665 and 750 nm was measured using a 90% acetone solution to auto-zero the spectrophotometer. After, two drops of 1N HCl was added to each sample, again measuring absorbance at 665 and 750 nm. Chlorophyll *a* and phaeopigment concentrations were then calculated using the following equations (Jeffrey & Humphrey 1975), where v is equal to the volume of the extract (6 ml) and A is equal to 10 divided by the area of the core:

$$\text{Chlorophyll } a = 26.7 * (((665_0 - 750_0) - (665_a - 750_a)) * v) * A \tag{3}$$

$$\text{Phaeopigments} = (26.7 * ((1.7 * (665_a - 750_a)) - (665_0 - 750_0)) * v) * A \tag{4}$$

Vegetation Characterization:

In July and October 2019, a 0.25 m^2 quadrat was placed at each ground-truth plot, and the total number of *S. alterniflora* culms within the plot was recorded. The height of the first 10 *S. alterniflora* culms along a diagonal transect between opposite corners of the quadrat were then measured to the tip of the tallest leaf, noting the presence of an inflorescence if applicable. The percent cover of each other species within the plot was evaluated to the nearest 5% interval; if percent cover was less than 5%, it was recorded to the nearest whole number instead.

Additionally, three *S. alterniflora* culms were clipped from near each ground-truth plot assessed in July and October 2019. These culms were dried at 60 °C for 24-48 hrs. and homogenized in an electric coffee mill, before being analyzed for carbon and nitrogen content using a Perkin Elmer 2400 Elemental Analyzer.

To establish an empirical relationship between *S. alterniflora* height and AGB, 201 culms were collected from throughout the marsh sites in July 2019, taking samples from near - but not within - the imaging scenes. Culms were clipped at the sediment surface and bagged. Sediment, detritus, and invertebrates on the plants were washed off in the laboratory. The height of each culm was then measured before drying at 60 °C for 24-48 hr, depending on the size of the culm, after which the mass of each culm was measured. A similar methodology was used to establish an empirical relationship for October 2019 for the young marsh only, with slight differences. Instead, 59 culms were collected from within the imaging scenes but outside of the ground-truth plots following the completion of imaging, to ensure a representative sample.

Second order polynomial regression equations were created to model *S. alterniflora* AGB as a function of culm height, using the height and respective dry AGB for the culms collected in July and October 2019. The regression models relating culm dry AGB (y) and height (x) for July and October 2019 were:

$$\text{July 2019: } y = 0.0005x^2 + 0.018x \ (R^2 = 0.87) \tag{1}$$

$$\text{October 2019: } y = 0.0003x^2 + 0.0205x \ (R^2 = 0.86) \tag{2}$$

Using *S. alterniflora* culm density and height data collected at each ground-truth plot, AGB density was estimated for each ground-truth plot by applying these empirical models (Figure 3). The average AGB per *S. alterniflora* culm within a plot was calculated using the 10 culm heights measured at each ground-truth plot in the field. After, AGB density was estimated by multiplying the average AGB per culm per plot by the number of culms per plot and by the plot size.

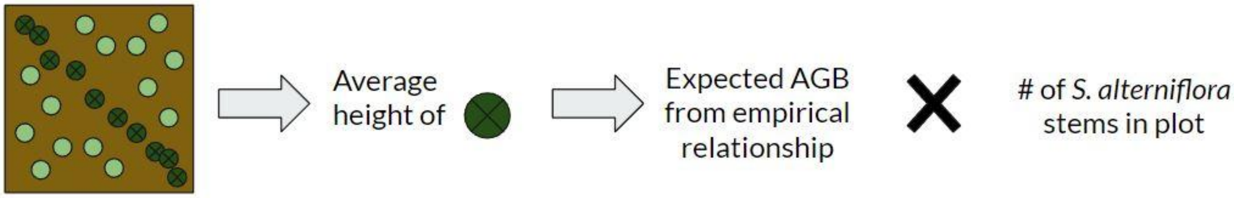

Figure 3: Illustration of AGB estimation process at each ground-truth plot in 2019. Using a representative sample of 10 *S. alterniflora* culm heights, an average height for the plot, and its expected AGB was calculated from the established empirical relationships (Equations 1 & 2). The expected AGB was then multiplied by the number of culms in the plot to estimate AGB.

Invertebrate Abundance Assessment:

Invertebrate surveys were performed at each ground-truth plot during the July 2019 field campaign. The number of *Littorina irrorata*, *Ilyanassa obsoleta*, *Crassostrea virginica,* and *Geukensia demissa* individuals were counted at each plot. The number of *Uca pugnax*, *Uca pugilator*, *Sesarma reticulatum*, and *Panopeus herbstii* was determined based on the number of burrows present, assuming one crab per burrow. The number of hooded and straight burrows were used to determine the number of *Sesarma reticulatum* / *Panopeus herbstii* (combined) and fiddler crabs, respectively. Additionally, the percent cover of *Crassostrea virginica* and *Geukensia demissa* were estimated for each plot.

Statistical Evaluation of Site Edaphic and Ecological Characteristics:

To evaluate similarities and differences between and within conditions observed at the Mature Marsh and the Young Marsh, two-way ANOVA tests were used to analyze sediment bulk density, SOM, C, N, P, and C:N at 1 cm and 10 cm depths. Afterwards, Tukey's HSD post hoc tests were used to perform pairwise comparisons. Two-sample t-tests were used to compare chlorophyll *a*, phaeopigments, and salinity between the two sites, as these were only collected at one depth. Additionally, two-sample t-tests were used to evaluate differences in *S. alterniflora* AGB, culm height, density, C, N, and C:N between the two sites. Bonnett and Levene's tests for equality of variance were used to compare variation in *S. alterniflora* AGB, height, and density between the sites.

Finally, Kruskal-Wallis tests were used to compare invertebrate abundance and percent cover between the two sites. This test was chosen because invertebrate counts were heavily skewed right for all distributions, due to the majority of plots containing few to no individuals, requiring a nonparametric test for comparison.

Digitization of Drone and Mast Ground-Truth Plots:

Ground-truth plots within the 2019 drone and mast-mounted imagery were digitized using ENVI software. For the drone imagery, the flags and PVC poles placed at the corners of each ground-truth plot were used to identify their boundaries during digitization (Figure 4A, B). However, if not all of the plot corners were clearly visible within the imagery, a simple linear translation was used to overlay the GPS coordinates of the ground-truth plot edges with the visible feature(s) (Figure 4C).

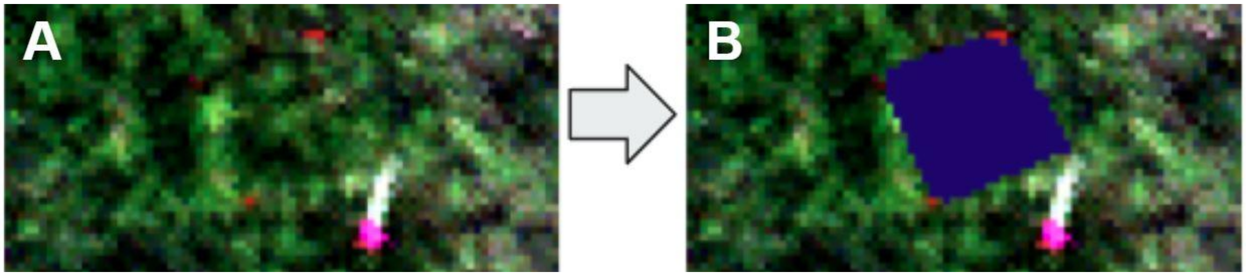

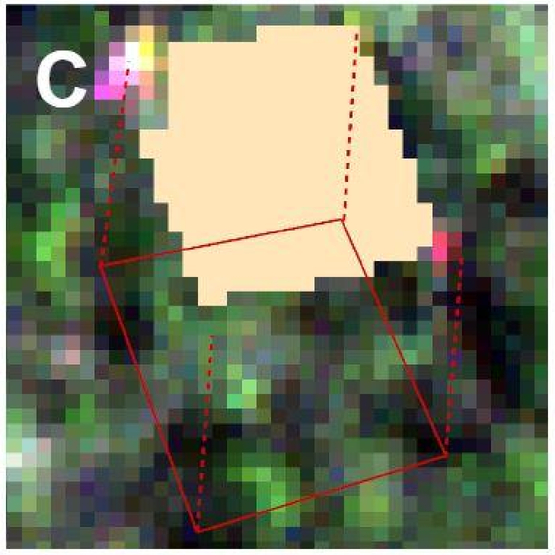

Figure 4: Drone imagery (A) and example of a digitized ground-truth plot (B). Here, three flags and the base of the PVC pole marking the plot were clearly visible, and were used to identify the corners of the plot. Figure 4C illustrates the process used to digitize ground-truth plots when not all of the corners were visible within the drone imagery. The solid red polygon represents the GPS coordinates taken at the corners of the plot, while the red dashed lines represent the translation vector used to overlay it onto the visible feature(s).

Ground-truth plots in the mast imagery were digitized using the flags and PVC poles visible in the imagery as a reference to form the boundaries of the ROIs, taking care to exclude plants outside of the plot in the foreground and background (Figure 5). If only one flag or pole was visible, a conservatively sized, representative sample of pixels was taken from around the visible feature using a rectangular ROI.

Figure 5: Example of the digitization process for ground-truth plots within the mast-mounted, obliquely angled hyperspectral imagery.

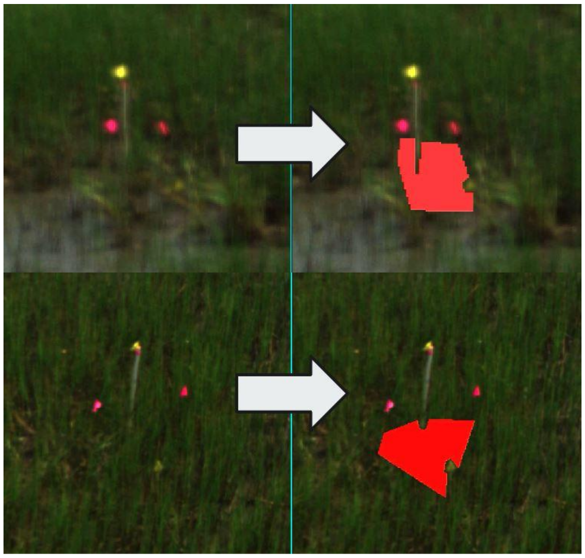

Only plots containing entirely *S. alterniflora*, or containing *S. alterniflora* and negligible quantities of other species (≤1% cover) were considered for further analysis. After removing these plots, and a single plot with a statistically significant high outlying value for *S alterniflora* AGB (Grubb's test, p<0.001), 47 plots at the Mature Marsh and 49 plots at the Young Marsh sites remained for analysis.

Regression Modeling of *S. alterniflora* AGB:

We calculated a selection of the most commonly used vegetation indices (VI; Table 1) from the mast-mounted (2 m and 6 m) and drone (50 m and 100 m) imagery collected in 2019, using ENVI's spectral indices tool. Spectral indices were also calculated for the 4 m mast-mounted imagery at the Young Marsh; however, this was not possible at the Mature Marsh because the camera angle for one imaging scene did not allow the ground-truth plots to be seen. Following digitization of all ground-truth plots at both drone resolutions and all mast camera heights considered, average VI values for each plot were extracted using ENVI ROI statistics.

Additionally, average spectra across all pixels within each ground-truth plot were extracted for all drone and mast elevations considered in July and October 2019.

For narrowband indices, the nearest wavelength present in the imagery, within an allowable tolerance range, was used. For broadband indices, the wavelength nearest the center of the spectral region indicated was used. To simulate and account for how splitting the data into training and testing sets affects the resulting regression models, 1000 linear regression models predicting AGB were created for each VI, using a random 75% of the data for creating the model for each run. Afterwards, the average and standard deviation of the 1000 regression constants and coefficients was calculated, along with average R^2, p-values, RMSE, and NRMSE. To identify a representative regression model to calculate plot level AGB, the model with NRMSE nearest the median NRMSE of the 1000 runs was chosen, illustrating the typical performance for each VI.

Table 1: Vegetation indices used for regression modeling of *S. alterniflora* AGB.

Index	Formula	Citation
DVI	$NIR - red$	Foley et al. 1998
GDVI	$NIR - green$	Sripada et al. 2005
GNDVI	$\frac{NIR - green}{NIR + green}$	Gitelson & Merzlyak 1998
GOSAVI	$\frac{NIR - green}{NIR + green + 0.16}$	Sripada et al. 2005
GRVI	$\frac{NIR}{green}$	Sripada et al. 2006
GSAVI	$1.5 * \frac{NIR - green}{NIR + green + 0.5}$	Sripada et al. 2005
IPVI	$\frac{NIR}{NIR + red}$	Crippen 1990
MCARI2	$\frac{1.5 * [\,2.5\,(R_{800} - R_{670}) - 1.3(R_{800} - R_{550})]}{\sqrt{(2R_{800}+1)^{2} - (6R_{800} - 5R_{670}) - 0.5}}$	Haboudane et al. 2004
MNLI	$\frac{1.5 * (NIR^{2} - red)}{NIR^{2} + red + 0.5}$	Yang et al. 2008
MSR	$\frac{(\frac{NIR}{red}) - 1}{\sqrt{\frac{NIR}{red}} + 1}$	Chen 1996
MSAVI2	$0.5 * [(2NIR + 1) - \sqrt{(2NIR + 1)^{2} - 8(NIR - red)}]$	Qi et al. 1994
MTVI2	$\frac{1.5 * [1.2(R_{800} - R_{550}) - 2.5(R_{670} - R_{550})]}{\sqrt{(2*R_{800}+1)^{2} - (6*R_{800} - 5*\sqrt{R_{670}}) - 0.5}}$	Haboudane et al. 2004
NLI	$\frac{NIR^{2} - red}{NIR^{2} + red}$	Goel & Qin 1994
NDVI	$\frac{(NIR - red)}{(NIR + red)}$	Martynenko et al. 2014
OSAVI	$\frac{(1 + 0.16)\,(R_{800} - R_{670})}{(R_{800} + R_{670} + 0.61)}$	Rondeaux et al. 1996
RENDVI	$\frac{R_{750} - R_{705}}{R_{750} + R_{705}}$	Gitelson & Merzlyak 1994, Sims & Gamon 2002

RDVI	$\frac{R_{800} - R_{670}}{\sqrt{R_{800} + R_{670}}}$	Roujean & Breon 1995
SR	$\frac{NIR}{red}$	Jordan 1969
TDVI	$\sqrt{0.5 + \frac{(NIR - red)}{(NIR + red)}}$	Bannari et al. 2002
TGI	$\frac{(red - blue)(red - green) - (red - green)(red - blue)}{2}$	Hunt et al. 2011
TVI	$\frac{120 * (R_{750} - R_{550}) - 200 * (R_{670} - R_{550})}{2}$	Broge & Leblanc 2000
VREI1	$\frac{R_{740}}{R_{720}}$	Vogelmann et al. 1993
VREI2	$\frac{R_{734} - R_{747}}{R_{715} + R_{726}}$	Vogelmann et al. 1993
WDRVI	$\frac{0.2 * NIR - red}{0.2 * NIR + red}$	Gitelson et al. 2004

Residual Analysis of *S. alterniflora* AGB Estimates:

Individual site regression model residuals were calculated from the difference between the model predicted AGB and field observed AGB values. Using forward stepwise multiple regression with a 95% confidence level to enter the model, plot-level physicochemical and ecological factors, including elevation, benthic chlorophyll and phaeopigments, edaphic properties, *S. alterniflora* tissue nutrients, culm density, and culm height were regressed against model residuals for the five highest R^2 models at the Mature and Young Marshes, to identify any correlations to these variables. Additionally, residuals were calculated for the three highest performing oblique AGB models at each site and were regressed against plot-level GSD, which is dependent on the elevation of the mast's hyperspectral sensor and distance to the plot.

Evaluation of Interseasonal Model Applicability:

Interseasonal applicability of AGB regression models was investigated by applying the five highest R^2 models for the Young Marsh in July 2019 to the imagery collected in October 2019. The 6 m mast elevation was chosen for this analysis, as it produced the most accurate regression models for the site in July 2019. Using the subset of plots resampled in the Young Marsh in October 2019, regression model results were validated using ground-truth AGB data. The accuracy of each model was evaluated by comparing RMSE and NRMSE values between months, and by observing the adherence of observed vs. predicted AGB values to a 1:1 line.

Results:

Characterization of Chronosequence Sites:

Significant differences were common among the edaphic characteristics measured at the Mature Marsh and Young Marsh sites (Table 2, Table 3, Table 4). BD was higher within the Young Marsh and increased with depth at both sites, but there was a significant interaction because of the much greater change with depth at the Young Marsh (Table 3, $p<0.001$ site*depth interaction). SOM, C, N, and P content were all significantly higher at the Mature Marsh site at both depths relative to the Young Marsh ($p<0.001$ for all site differences). While SOM, N, and total P all decreased with depth at both sites ($p\leq0.001$ for all for depth), sediment C decreased significantly with depth at the Young Marsh site, but not at the Mature Marsh (ANOVA $p=0.012$ for site*depth interaction). Additionally, while sediment C:N increased with depth at both sites, significant differences were only observed between sites at a 10 cm depth (ANOVA $p<0.001$ for site*depth interaction). Although Chlorophyll *a* concentrations were not significantly different between sites ($p=0.72$, Table 4), phaeopigment concentrations were significantly higher at the Mature Marsh ($p<0.001$). Finally, porewater salinity was significantly higher at the Young Marsh site ($p<0.001$).

Table 2: Sediment, plant, and invertebrate community characteristics of the two salt marsh chronosequence sites. An asterisk in the central column indicates a significant difference between the two sites at a 95% confidence level. Superscript letters adjacent to means represent grouping information for means tested with Tukey's HSD at a 95% confidence level; means that do not share a letter are significantly different from one another.

	Mature Marsh			Young Marsh	
Sediment Characteristics	Mean ± Std. Dev.	Min - Max		Mean ± Std. Dev.	Min - Max
Bulk Density 0-1cm (g/m^2)	0.46^{a} ± 0.15	0.30 - 0.92	*	1.09^{c} ± 0.22	0.43 - 1.48
Bulk Density 0-10cm (g/m^2)	0.68^{b} ± 0.14	0.43 - 1.18	*	1.66^{d} ± 0.42	0.99 - 2.82
SOM 0-1cm (%)	8.54^{a} ± 1.22	5.07 - 10.76	*	2.83^{b} ± 1.77	0.70 - 10.69
SOM 0-10cm (%)	8.06^{a} ± 1.32	3.29 - 10.97	*	2.04^{c} ± 0.94	0.71 - 4.57
C 0-1cm (%)	2.72^{a} ± 0.69	1.33 - 5.35	*	0.82^{b} ± 0.66	0.17 - 3.28
C 0-10cm (%)	2.85^{a} ± 0.54	0.95 - 4.30	*	0.57^{b} ± 0.33	0.11 - 1.46
N 0-1cm (%)	0.255^{a} ± 0.066	0.095 - 0.375	*	0.077^{c} ± 0.058	0.020 - 0.300
N 0-10cm (%)	0.205^{b} ± 0.044	0.055 - 0.290	*	0.048^{d} ± 0.025	0.010 - 0.125
C:N 0-1cm	10.96^{ab} ± 2.03	8.29:1 - 16.67		10.5^{a} ± 1.64	7.83 - 16.40
C:N 0-10cm	14.16^{c} ± 2.12	11.12:1 - 19.27	*	11.51^{b} ± 1.92	6.2 - 16.67
P 0-1cm (µg/g)	710.7^{a} ± 102.5	488.2 - 960.6	*	375.7^{c} ± 143.2	176.6 - 929.7
P 0-10cm (µg/g)	643.0^{b} ± 104.0	295.8 - 924.9	*	300.4^{d} ± 69.4	176.9 - 471.5
Chlorophyll *a* 0-1cm (mg/m^2)	112.4 ± 57.4	35.8 - 259.6		109.0 ± 38.6	43.9 - 210.3
Phaeopigments 0-1cm (mg/m^2)	107.8 ± 30.0	59.3 - 175.2	*	76.8 ± 56.6	10.0 - 300.0
Salinity (ppt)	37 ± 2	34 - 41	*	41 ± 5	30 - 56
Plant Characteristics	**Mean** ± Std. Dev.	Min - Max		**Mean** ± Std. Dev.	Min - Max
S. alterniflora AGB (g/m^2)	508 ± 342.4	6.7 - 1346.6		440.1 ± 264.6	0 - 1083.5
S. alterniflora culm height (cm)	60.6 ± 16.5	4.2 - 121		60.6 ± 27.5	4.5 - 140
S alterniflora density (culms/m^2)	145 ± 63.5	4 - 288		144.2 ± 61.4	0 - 296
S. alterniflora C (%)	40.9 ± 1.9	37.8 - 43.9		40.9 ± 1.1	38.1 - 43.7
S. alterniflora N (%)	0.81 ± 0.11	0.610 - 1.10	*	0.86 ± 0.12	0.610 - 1.15
S. alterniflora C:N	51.46 ± 6.98	35.4:1 - 66.6		48.83 ± 7.48	34.88 - 67.1
Invertebrate Communities	**Mean** ± Std. Dev.	Min - Max		**Mean** ± Std. Dev.	Min - Max
Ilyanassa obsoleta (#)	18 ± 24	0 - 92	*	3 ± 9	0 - 49
Littoraria irrorata (#)	6 ± 6	0 - 28	*	12 ± 14	0 - 57
Hooded Crabs (#)	0.1 ± 0.4	0 - 2		0.2 ± 0.5	0 - 3
Fiddler Crabs (#)	4 ± 7	0 - 33	*	16 ± 21	0 - 101
Crassostrea virginica (#)	3 ± 5	0 - 27		2 ± 4	0 - 17
Oyster cover (%)	2 ± 3	0 - 10		1 ± 3	0 - 10
Geukensia demissa (#)	6 ± 21	0 - 105		2 ± 6	0 - 33
Geukensia demissa cover (%)	4 ± 12	0 - 65		1 ± 4	0 - 25

Table 3: Two-way ANOVA results testing the effects of site (Mature Marsh, Young Marsh) and depth (1 cm, 10 cm) on sediment characteristics. Bold p-values indicate significant effects at a 95% confidence level. For all F-statistics, df1 = 3, and df2 = 212.

	Site		**Depth**		**Site * Depth**	
	F	*p*	F	*p*	F	*p*
Bulk Density	486.83	**<0.001**	117.6	**<0.001**	24.21	**<0.001**
SOM	1002.01	**<0.001**	11.79	**0.001**	0.68	0.412
%C	725.37	**<0.001**	0.64	0.424	6.36	**0.012**
%N	594.86	**<0.001**	32.56	**<0.001**	2.12	0.147
C:N	34.87	**<0.001**	64.11	**<0.001**	17.3	**<0.001**
P	520.3	**<0.001**	23.16	**<0.001**	0.06	0.800

Table 4: Two-sample t-tests comparing sediment and *S. alterniflora* characteristics, and Kruskal-Wallis tests comparing invertebrate community characteristics between sites. Bold p-values indicate significant effects at a 95% confidence level. Equal variances were not assumed for two-sample t-tests.

	t	df	*p*
Chlorophyll a 0-1 cm (mg/m^2)	3.45	78	0.722
Phaeopigments 0-1cm (mg/m^2)	3.65	93	**<0.001**
Salinity (ppt)	-4.73	73	**<0.001**
S. alterniflora AGB (g/m^2)	1.08	86	0.284
S. alterniflora culm height (cm)	-0.004	79	0.996
S alterniflora density ($culms/m^2$)	0.06	93	0.952
S. alterniflora C (%)	0.01	73	0.991
S. alterniflora N (%)	-2.11	105	**0.037**
S. alterniflora C:N	1.88	103	0.063

	χ2	df	*p*
Ilyanassa obsoleta (#)	20.448	1	**<0.001**
Littoraria irrorata (#)	0.955	1	0.329
Hooded Crabs (#)	0.334	1	0.563
Fiddler Crabs (#)	10.617	1	**0.001**
Crassostrea virginica (#)	6.978	1	**0.008**
Oyster cover (%)	7.470	1	**0.006**
Geukensia demissa (#)	0.0147	1	0.903
Geukensia demissa cover (%)	0.0433	1	0.835

Fewer significant differences were observed within the *S. alterniflora* communities present at the Mature Marsh and the Young Marsh sites (Table 2). Between the two sites, there were no significant differences in *S. alterniflora* AGB (p=0.28), culm height (p=0.99), culm density (p=0.95), or C content (p=0.99). However, the standard deviation of *S. alterniflora* culm heights was significantly higher at the Young Marsh (Bonnett test, p<0.001, Levene test p<0.001), while the standard deviation of *S. alterniflora* AGB at the Mature Marsh was significantly higher only at a 90% significance level (Bonnett test, p<0.086, Levene test p<0.063), suggesting that variability is caused by differing plant morphologies. *S. alterniflora* N content was significantly higher at the Young Marsh site (p=0.037), and C:N ratios were significantly higher at the Mature Marsh at a 90% confidence level, while nearing significance at 95% (p=0.06). However, no significant differences were observed in *S. alterniflora* C content (p=0.99) between the two sites. While not reflected in Table 2, it should be noted that the Young Marsh site also contained *Salicornia virginica*, *Limonium* spp., and *Spartina patens* in the high marsh plots, which were excluded from regression modeling.

Invertebrate communities were highly variable within and between sites (Table 2, Table 4). All abundance distributions were heavily right skewed, with the majority of plots surveyed containing few to no individuals. *Ilyanassa obsoleta* abundance was significantly higher at the Mature Marsh (Kruskal-Wallis p<0.001), while fiddler crab abundance (Kruskal-Wallis p=0.001), *Crassostrea virginica* abundance (Kruskal-Wallis p=0.008) and oyster percent cover (Kruskal-Wallis p=0.006) were significantly higher at the Young Marsh. No significant differences were observed in *Littoraria irrorata* abundance (Kruskal-Wallis p=0.33), hooded crab abundance (Kruskal-Wallis p=0.56), *Geukensia demissa* abundance (Kruskal-Wallis p=0.90), and *Geukensia demissa* percent cover (Kruskal-Wallis p=0.84) between the two sites.

Regression Modeling of *S. alterniflora* AGB:

Average reflectance spectra from the 2019 ground-truth plots resembled typical spectral characteristics of vegetation (Figure 6, Figure 7). Plot-level reflectance spectra demonstrated a relatively high level of similarity between the two resolutions collected from the Mature Marsh (Figure 6). However, major differences were observed between plot-level spectra collected at the Young Marsh, where the 50 m spectra typically demonstrated higher reflectance values across the visible-NIR region, with steeper red-edge slopes compared to the 100 m spectra and much greater variability among the different plots (Figure 6). Visible blue and red absorption features - and high green reflectance - were more pronounced in the oblique spectra (Figure 7) than in the nadir spectra (Figure 6). Additionally, red-edge slopes were steeper, and NIR reflectance higher in the oblique imagery, when compared to nadir views.

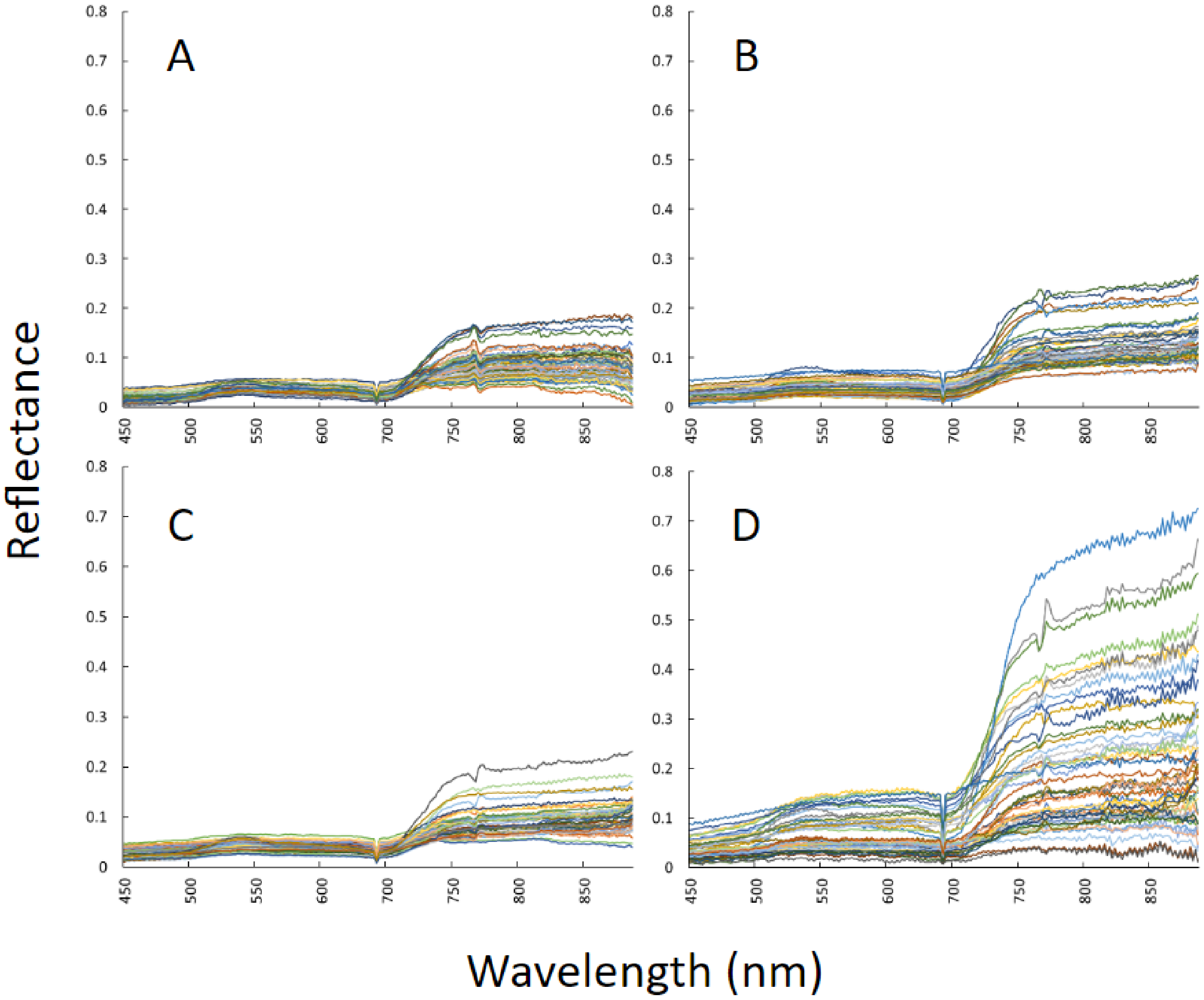

Figure 6: Average reflectance spectra collected from the ground-truth plots in the Mature (A, C) and Young Marsh (B, D) in July 2019, using the MX-1 UAS system at two elevations: 100 m (A, B), and 50 m (C, D).

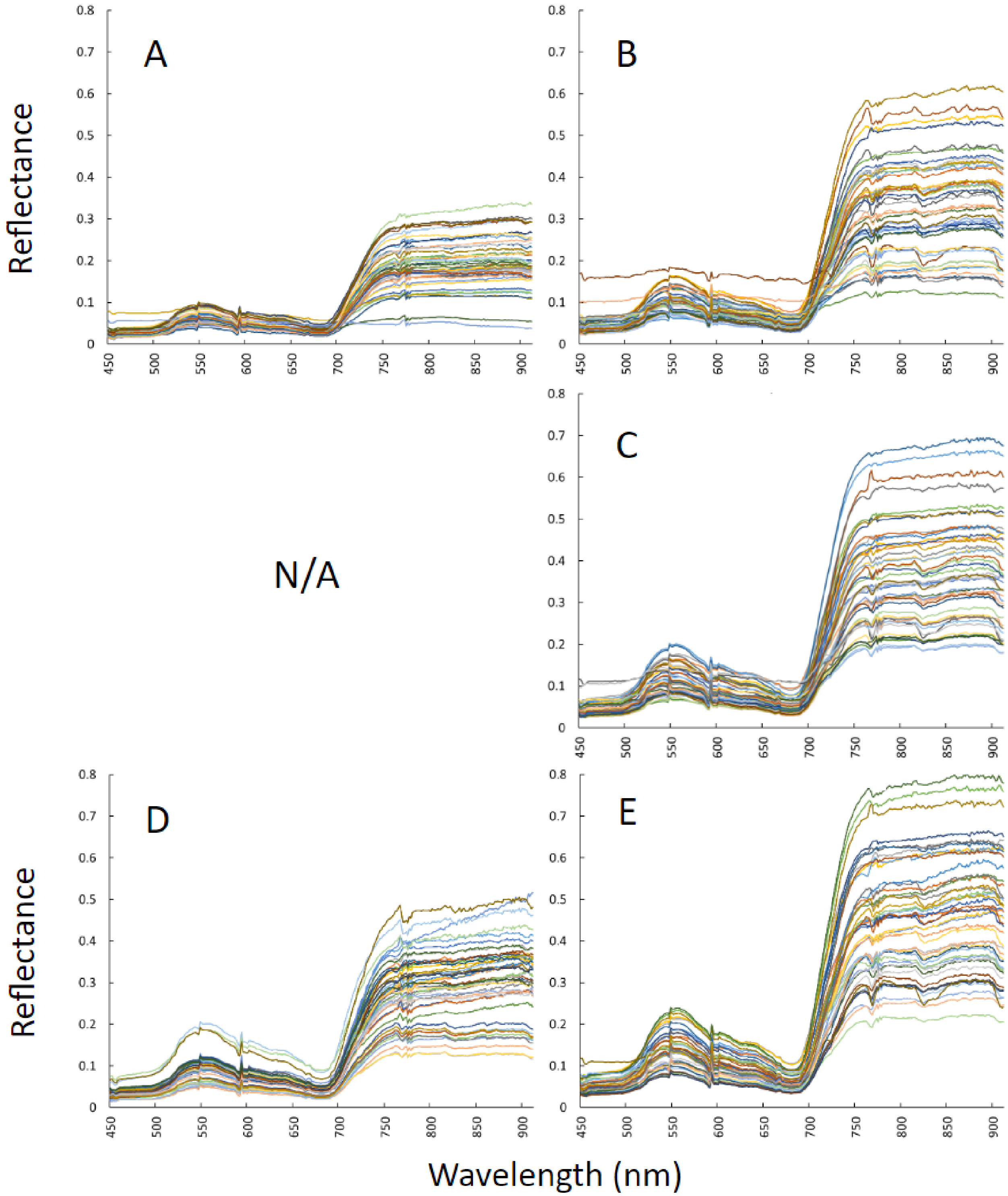

Figure 7: Average reflectance spectra collected from the ground-truth plots in the Mature (A, D) and Young Marshes (B, C, E) in July 2019, using the Headwall VNIR Micro-Hyperspec High Efficiency E-series system to collect obliquely angled imagery at 6 m (A, B), 4 m (C), and 2 m (D, E) camera elevations.

All regression models for nadir imagery collected by UAS were significant at a 95% confidence level (Table 5, Table 6). The highest performing models based on R^2 and NRMSE were obtained using 3 cm nadir imagery, however, average model performance across all indices was comparable between 3 cm and 6 cm nadir imagery for both individual site and combined models. Typically, combined site models performed worse than individual site models, with the exception being that average performance was similar for combined and Young Marsh 6 cm models. Across almost every index evaluated, nadir regression model performance was higher at the Mature Marsh site, with R^2 values averaging 0.27 and 0.30 higher at the Mature Marsh than the model counterparts at the Young Marsh, for 6 cm and 3 cm imagery, respectively.

Table 5: R^2 values of the representative linear regression models obtained from the 1000 simulated subset models. Empty gray cells indicate instances where the representative model was not a significant predictor at a 95% confidence level for that combination of VI and imagery. Dashed outlines indicate the five highest R^2 models for the combined and individual site models.

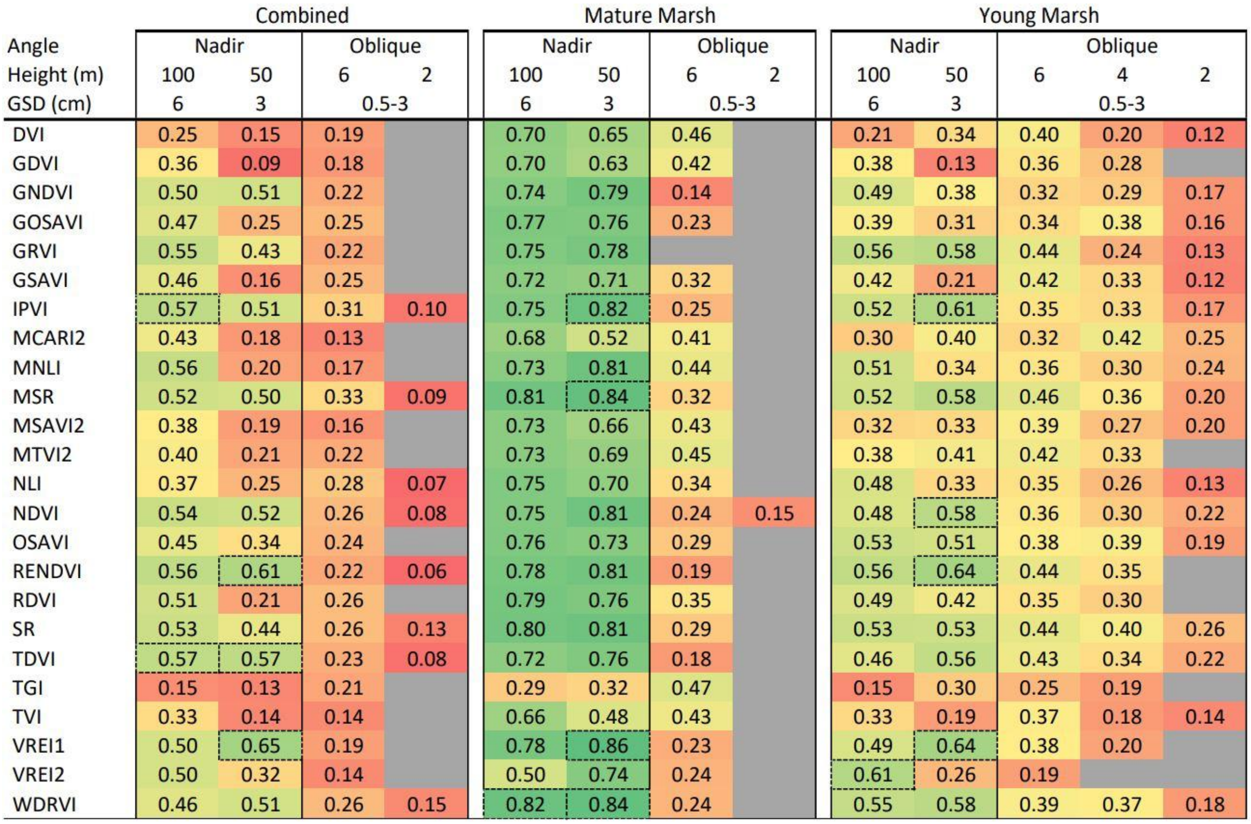

	Combined				Mature Marsh				Young Marsh				
Angle	Nadir		Oblique		Nadir		Oblique		Nadir		Oblique		
Height (m)	100	50	6	2	100	50	6	2	100	50	6	4	2
GSD (cm)	6	3	0.5-3		6	3	0.5-3		6	3	0.5-3		
DVI	0.25	0.15	0.19		0.70	0.65	0.46		0.21	0.34	0.40	0.20	0.12
GDVI	0.36	0.09	0.18		0.70	0.63	0.42		0.38	0.13	0.36	0.28	
GNDVI	0.50	0.51	0.22		0.74	0.79	0.14		0.49	0.38	0.32	0.29	0.17
GOSAVI	0.47	0.25	0.25		0.77	0.76	0.23		0.39	0.31	0.34	0.38	0.16
GRVI	0.55	0.43	0.22		0.75	0.78			0.56	0.58	0.44	0.24	0.13
GSAVI	0.46	0.16	0.25		0.72	0.71	0.32		0.42	0.21	0.42	0.33	0.12
IPVI	0.57	0.51	0.31	0.10	0.75	0.82	0.25		0.52	0.61	0.35	0.33	0.17
MCARI2	0.43	0.18	0.13		0.68	0.52	0.41		0.30	0.40	0.32	0.42	0.25
MNLI	0.56	0.20	0.17		0.73	0.81	0.44		0.51	0.34	0.36	0.30	0.24
MSR	0.52	0.50	0.33	0.09	0.81	0.84	0.32		0.52	0.58	0.46	0.36	0.20
MSAVI2	0.38	0.19	0.16		0.73	0.66	0.43		0.32	0.33	0.39	0.27	0.20
MTVI2	0.40	0.21	0.22		0.73	0.69	0.45		0.38	0.41	0.42	0.33	
NLI	0.37	0.25	0.28	0.07	0.75	0.70	0.34		0.48	0.33	0.35	0.26	0.13
NDVI	0.54	0.52	0.26	0.08	0.75	0.81	0.24	0.15	0.48	0.58	0.36	0.30	0.22
OSAVI	0.45	0.34	0.24		0.76	0.73	0.29		0.53	0.51	0.38	0.39	0.19
RENDVI	0.56	0.61	0.22	0.06	0.78	0.81	0.19		0.56	0.64	0.44	0.35	
RDVI	0.51	0.21	0.26		0.79	0.76	0.35		0.49	0.42	0.35	0.30	
SR	0.53	0.44	0.26	0.13	0.80	0.81	0.29		0.53	0.53	0.44	0.40	0.26
TDVI	0.57	0.57	0.23	0.08	0.72	0.76	0.18		0.46	0.56	0.43	0.34	0.22
TGI	0.15	0.13	0.21		0.29	0.32	0.47		0.15	0.30	0.25	0.19	
TVI	0.33	0.14	0.14		0.66	0.48	0.43		0.33	0.19	0.37	0.18	0.14
VREI1	0.50	0.65	0.19		0.78	0.86	0.23		0.49	0.64	0.38	0.20	
VREI2	0.50	0.32	0.14		0.50	0.74	0.24		0.61	0.26	0.19		
WDRVI	0.46	0.51	0.26	0.15	0.82	0.84	0.24		0.55	0.58	0.39	0.37	0.18

Table 6: NRMSE values of the representative linear regression models obtained from the 1000 simulated subset models. Empty gray cells indicate instances where the representative model was not a significant predictor at a 95% confidence level for that combination of VI and imagery. Dashed outlines indicate the five lowest NRMSE models for the combined and individual site models.

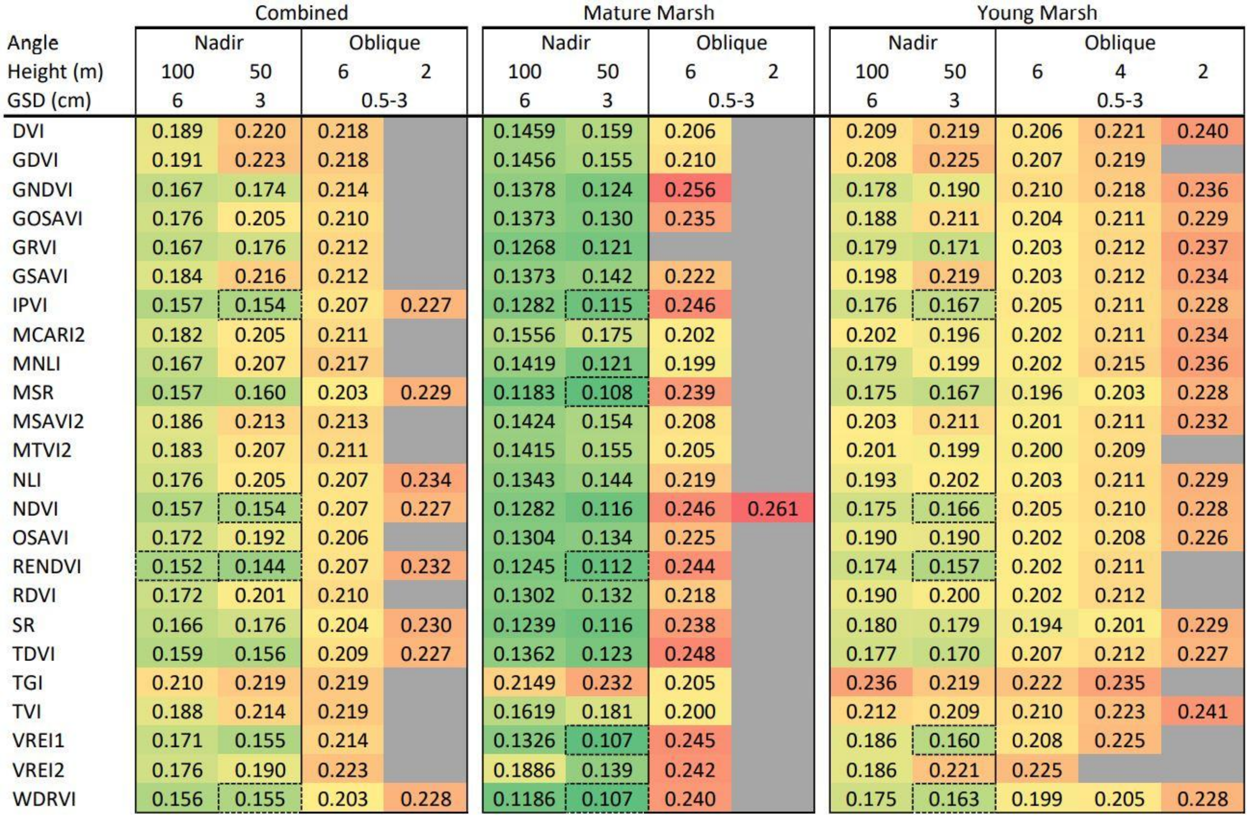

	Combined				Mature Marsh				Young Marsh				
Angle	Nadir		Oblique		Nadir		Oblique		Nadir		Oblique		
Height (m)	100	50	6	2	100	50	6	2	100	50	6	4	2
GSD (cm)	6	3	0.5-3		6	3	0.5-3		6	3	0.5-3		
DVI	0.189	0.220	0.218		0.1459	0.159	0.206		0.209	0.219	0.206	0.221	0.240
GDVI	0.191	0.223	0.218		0.1456	0.155	0.210		0.208	0.225	0.207	0.219	
GNDVI	0.167	0.174	0.214		0.1378	0.124	0.256		0.178	0.190	0.210	0.218	0.236
GOSAVI	0.176	0.205	0.210		0.1373	0.130	0.235		0.188	0.211	0.204	0.211	0.229
GRVI	0.167	0.176	0.212		0.1268	0.121			0.179	0.171	0.203	0.212	0.237
GSAVI	0.184	0.216	0.212		0.1373	0.142	0.222		0.198	0.219	0.203	0.212	0.234
IPVI	0.157	0.154	0.207	0.227	0.1282	0.115	0.246		0.176	0.167	0.205	0.211	0.228
MCARI2	0.182	0.205	0.211		0.1556	0.175	0.202		0.202	0.196	0.202	0.211	0.234
MNLI	0.167	0.207	0.217		0.1419	0.121	0.199		0.179	0.199	0.202	0.215	0.236
MSR	0.157	0.160	0.203	0.229	0.1183	0.108	0.239		0.175	0.167	0.196	0.203	0.228
MSAVI2	0.186	0.213	0.213		0.1424	0.154	0.208		0.203	0.211	0.201	0.211	0.232
MTVI2	0.183	0.207	0.211		0.1415	0.155	0.205		0.201	0.199	0.200	0.209	
NLI	0.176	0.205	0.207	0.234	0.1343	0.144	0.219		0.193	0.202	0.203	0.211	0.229
NDVI	0.157	0.154	0.207	0.227	0.1282	0.116	0.246	0.261	0.175	0.166	0.205	0.210	0.228
OSAVI	0.172	0.192	0.206		0.1304	0.134	0.225		0.190	0.190	0.202	0.208	0.226
RENDVI	0.152	0.144	0.207	0.232	0.1245	0.112	0.244		0.174	0.157	0.202	0.211	
RDVI	0.172	0.201	0.210		0.1302	0.132	0.218		0.190	0.200	0.202	0.212	
SR	0.166	0.176	0.204	0.230	0.1239	0.116	0.238		0.180	0.179	0.194	0.201	0.229
TDVI	0.159	0.156	0.209	0.227	0.1362	0.123	0.248		0.177	0.170	0.207	0.212	0.227
TGI	0.210	0.219	0.219		0.2149	0.232	0.205		0.236	0.219	0.222	0.235	
TVI	0.188	0.214	0.219		0.1619	0.181	0.200		0.212	0.209	0.210	0.223	0.241
VREI1	0.171	0.155	0.214		0.1326	0.107	0.245		0.186	0.160	0.208	0.225	
VREI2	0.176	0.190	0.223		0.1886	0.139	0.242		0.186	0.221	0.225		
WDRVI	0.156	0.155	0.203	0.228	0.1186	0.107	0.240		0.175	0.163	0.199	0.205	0.228

Obliquely angled imagery was typically outperformed by both nadir resolutions, for individual sites and when combined. For oblique imagery captured at 6 m and 4 m elevations, all but two regression models were significant (GRVI at the Mature Marsh and VREI2 at the Young Marsh, respectively). However, a large number of the 2 m elevation oblique imagery regression models were not significant for both sites individually, or for both sites combined. While some 6 m oblique models were able to outperform lower performance nadir models (ex. Mature Marsh TGI), the highest performing models overall were still obtained from nadir imagery. Models derived from obliquely angled imagery decreased in performance as mast elevation and viewing angle decreased, demonstrated by lower R^2 values, higher NRMSE values, and a reduced number of significant models at the 2 m elevation compared to the 6 m elevation. At the Young Marsh, where an intermediate, 4 m mast elevation was available for analysis, average model performance across all indices was typically between that of the 6 m and 2 m mast elevations, in terms of R^2 and NRMSE (Table 5, Table 6), implying that mast height and viewing angle are critical factors for model performance.

For both 3 cm and 6 cm nadir imagery, a large number of indices provided AGB models with high R^2 and low NRMSE at the Mature Marsh site. Comparatively, relatively few VIs provided high performance for the Young Marsh and combined site models. Across the individual site nadir models, IPVI, MSR, VREI1, and WDRVI provided the highest performance at the Mature Marsh, while IPVI, NDVI, RENDVI, VREI1, and VREI2 provided the highest performance at the Young Marsh. Similarly, IPVI, RENDVI, and VREI1 yielded the strongest combined site models, with TDVI also performing well (Table 7).

Table 7: Highest R^2 representative AGB regression models for the Mature Marsh, Young Marsh, and both sites combined. For all categories, 3 cm nadir resolution provided the highest R^2 model.

Mature Marsh	Model	R^2	RMSE
3 cm, nadir	$AGB = VREI1 * 2208.76 - 2165.49$	0.86	143.75
3 cm, nadir	$AGB = WDRVI * 1585.73 - 1035.58$	0.85	118.99
3 cm, nadir	$AGB = MSR * 697.55 - 41.37$	0.84	144.58
3 cm, nadir	$AGB = IPVI * 3638.46 - 1987.25$	0.82	154.61
6 cm, nadir	$AGB = WDRVI * 1557.88 - 973.49$	0.82	158.91

Young Marsh	Model	R^2	RMSE
3 cm, nadir	$AGB = RENDVI * 1929.18 - 46.61$	0.64	169.99
3 cm, nadir	$AGB = VREI1 * 1412.45 - 1408.07$	0.64	173.89
3 cm, nadir	$AGB = IPVI * 2710.85 - 1585.68$	0.61	157.30
6 cm, nadir	$AGB = VREI2 * -6570.82 + 94.53$	0.61	173.16
3 cm, nadir	$AGB = NDVI * 1479.60 - 259.89$	0.58	180.19

Combined	Model	R^2	RMSE
3 cm, nadir	$AGB = VREI1 * 1574.60 - 1512.85$	0.65	191.70
3 cm, nadir	$AGB = RENDVI * 2041.46 + 4.59$	0.61	193.61
6 cm, nadir	$AGB = IPVI * 2635.23 - 1453.5$	0.59	210.78
3 cm, nadir	$AGB = TDVI * 2661.64 - 2067.61$	0.57	209.29
6 cm, nadir	$AGB = TDVI * 2515.41 - 1998.8$	0.57	214.14

Residual Analysis of *S. alterniflora* AGB Estimates:

Of the 10 highest performing AGB models from the Mature and Young Marsh sites, nine had residuals positively correlated with *S. alterniflora* height, while seven had residuals positively correlated with *S. alterniflora* density (Table 8). At the Mature Marsh, all model residuals were negatively correlated with elevation. At the Young Marsh, residuals from four models were positively correlated with 10 cm sediment C:N, and three models were negatively correlated with bulk density at a 10 cm depth. Other ecological and edaphic characters were occasionally significant predictors of model residuals as well, including *S. alterniflora* tissue C:N, sediment C:N at a 1 cm depth, and benthic chlorophyll *a* concentrations. For oblique models, there were no significant relationships between GSD and model residuals at either site.

Table 8: Significant predictors of AGB model residuals and their regression coefficients, found through forward stepwise regression. Empty cells indicate the predictor was not significant at a 95% confidence level.

Model	Constant	*S. alt.* height (cm)	*S. alt.* density (#/m^2)	*S. alt.* C:N	Elev. (m)	Sediment C:N, 1cm	Sediment C:N, 10cm	Benthic Chl. *a* (mg/m^2)	BD 1cm (g/m^2)
Mature 3 cm, nadir IPVI	-286.7	3.76			-497				
Mature 3 cm, nadir MSR	-46.9	5.34			-444	-28.14			
Mature 3 cm, nadir VREI1	-388.7	4.24			-575			0.734	
Mature 3 cm, nadir WDRVI	-120.6	4.92	0.681		-498	-26.90			
Mature 6 cm, nadir WDRVI	-10.9		0.794		-748				
Young 3 cm, nadir IPVI	-547	3.07	1.51				32		-198.3
Young 3 cm, nadir NDVI	-586	2.58	1.45				35		-187.2
Young 3 cm, nadir RENDVI	-674	1.79	1.23	206			26.7		-154.2
Young 3 cm, nadir VREI1	-621	2.19	1.48				23.7		
Young 6 cm, nadir VREI2	-701	2.05	1.31	291					

Evaluation of Interseasonal Model Applicability:

Average reflectance spectra collected from ground-truth plots in the Young Marsh in July and October 2019 demonstrated major differences consistent with phenological changes occurring between seasons. For the subset of plots imaged in October, red reflectance in the 650-700 nm range increased compared to July, while NIR reflectance decreased somewhat, resulting in shallower red-edge slopes (Figure 8). Additionally, while green reflectance remained approximately the same between seasons, the slope of the spectra between the visible blue and green became shallower, and when combined with the increased red reflectance seen in October, results in less pronounced visible green reflectance.

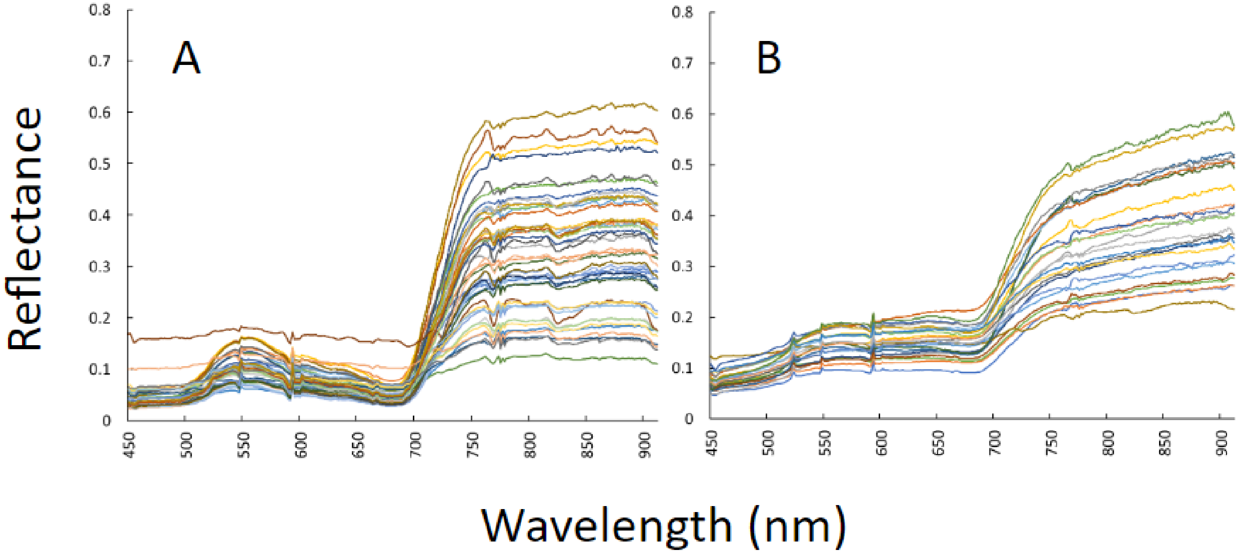

Figure 8: Reflectance spectra collected from the Young Marsh in July (A) and October 2019 (B), using the Headwall VNIR Micro-Hyperspec High Efficiency E-series system to collect obliquely angled imagery at a 6 m elevation.

Regression model predictions of *S. alterniflora* AGB were generally poor for the subset of plots resampled from the Young Marsh in October 2019, demonstrating markedly increased RMSE and NRMSE for four of the five models tested (Table 9), with October AGB estimates deviating heavily from the 1:1 line for those models (Figure 9).

Table 9: RMSE and NRMSE values for select 6 m oblique models applied between months at the Young Marsh.

Model	RMSE July	RMSE October	NRMSE July	NRMSE October
GRVI	190.03	154.88	0.236	0.187
MSR	186.16	270.74	0.270	0.632
RENDVI	193.77	325.08	0.280	1.544
TDVI	187.95	249.73	0.262	1.206
SR	189.96	269.90	0.274	1.948

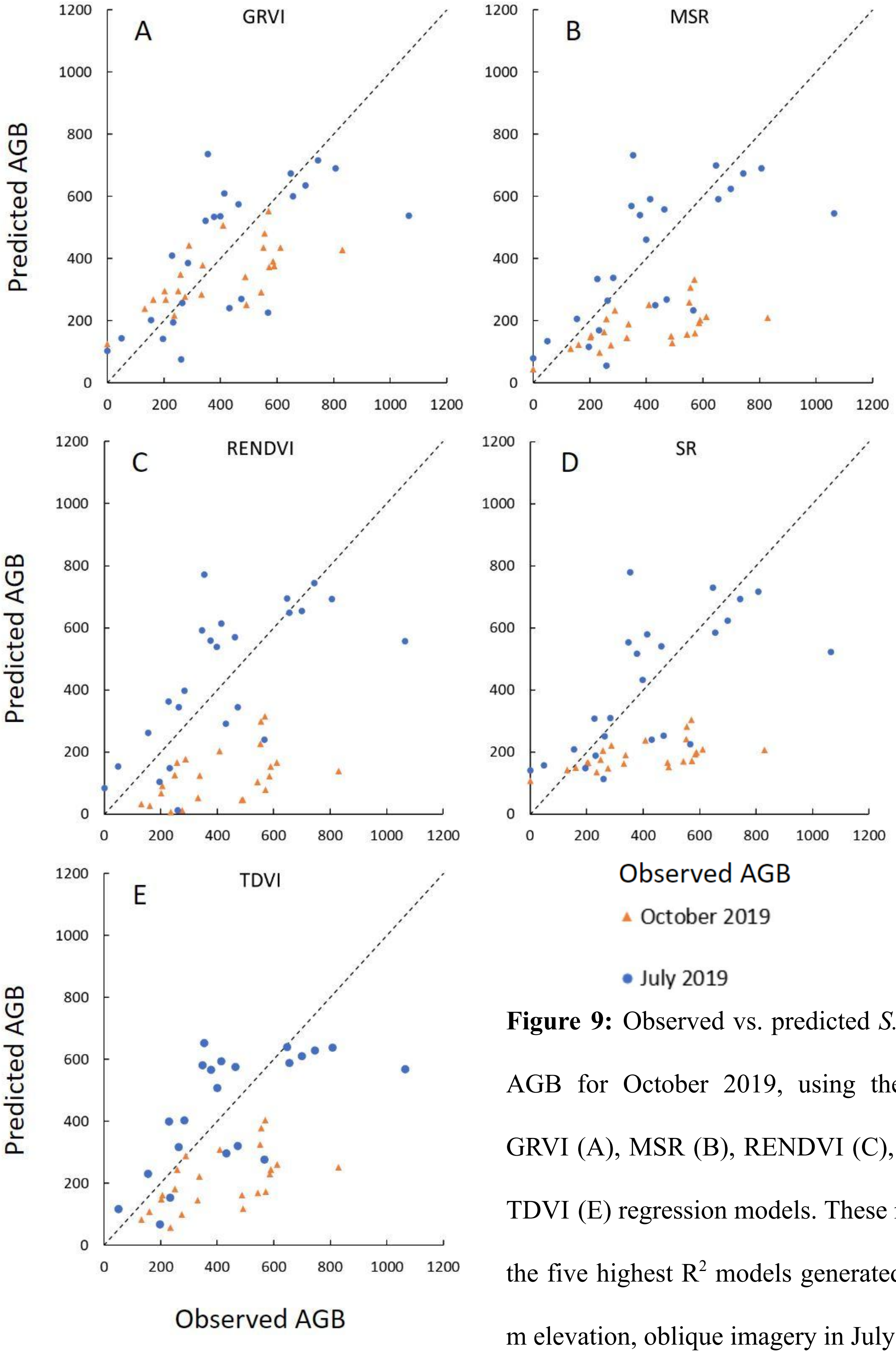

Figure 9: Observed vs. predicted *S. alterniflora* AGB for October 2019, using the July 2019 GRVI (A), MSR (B), RENDVI (C), SR (D), and TDVI (E) regression models. These models were the five highest R^2 models generated using the 6 m elevation, oblique imagery in July 2019.

For the four models with increased RMSE and NRMSE from July to October 2019 (MSR, RENDVI, RDVI, SR), the majority of plot level AGB predictions were lower than the AGB values measured in the field (Figure 9). However, October 2019 AGB estimates made using the GRVI July 2019 regression model adhered to the 1:1 line, and featured lower RMSE and NRMSE than the same plots in July 2019 (Figure 9).

Discussion:

Characterization of Chronosequence Sites:

With marsh age in this context being determined by when *S. alterniflora* recolonized an area after an overwash event, where large amounts of sand are deposited over an existing marsh, the differences in edaphic characteristics observed at the two chronosequence sites are expected and consistent with previous work at these sites (Goldsmith 2019, Osgood & Zieman 1993, Tyler & Zieman 1999, Walsh 1998). Marsh age, and the resulting differences it drives in SOM (He et al. 2016, Morgan & Short 2002, Osgood & Zieman 1993, Tyler et al. 2003, Walsh 1998) is likely the main factor in the differences observed between and within the two sites in terms of BD and sediment CNP (He et al. 2016, Tyler & Zieman 1999, Walsh 1998). Due to the Young Marsh's age, there has been less time for plants to grow, die, and decompose at the site, resulting in lower SOM at both depths than at the same depths measured at the Mature Marsh site. Additionally, the deposition of decaying plant material and trapping of fine organic-rich sediments (Christiansen et al. 2000, Stumpf 1983) brought in with the tide on the sediment surface explains the higher SOM in the top centimeter of sediment, relative to the 10 cm depth for both sites. Because SOM is nutrient rich, this same trend is observed for sediment N and P: higher nutrient concentrations are observed at the surface than at the 10 cm depth, and higher concentrations are observed at the Mature Marsh than at the Young Marsh.

SOM and sand fraction also likely explain the difference in BD between and within these two sites. With low BD SOM accumulating first at the sediment surface, lower BD values are seen in the top cm than at the 10 cm depth for both sites. Additionally, the high BD of sand, with less SOM to reduce BD, results in the Young Marsh having higher bulk densities at both depths observed, relative to the Mature Marsh. Furthermore, sediment silt and clay content have been observed increasing with marsh age (Goldsmith 2019, Tyler & Zieman 1999, Walsh 1998), further contributing to the low BD seen at the mature marsh.

While Tyler et al. (2003) and Goldsmith (2019) both found significantly higher chlorophyll *a* concentrations in younger salt marshes, chlorophyll *a* concentrations were not significantly different between the two sites in this study. It may be that a combination of (a)biotic factors supported an isolated algal bloom and/or high algal community productivity in 2019, resulting in the similar chlorophyll *a* values observed between sites here. However, the Mature Marsh contained significantly higher concentrations of phaeopigments, a degradation product of chlorophyll, at the sediment surface. Given the age of the Mature Marsh, this is likely because there have been decades more time for algal communities to develop and die off at the site, allowing the chlorophyll contained to degrade and accumulate over time within the sediment.

While there were no significant differences in *S. alterniflora* AGB, culm height, or density between the two sites, higher variance in culm height was observed at the Young Marsh.

With the Young Marsh encompassing areas from -60 cm below to +41 cm above sea level, and with greater variability in elevation compared to the Mature Marsh, the increased variance in culm height at this site can likely be attributed to the varying phenotypic expression of *S. alterniflora* at different elevations. Additionally, the higher average elevation and presence of plots located closer to the high marsh and upland at the Young Marsh likely leads to the higher salinity observed at this site, as these areas are less frequently and completely inundated, resulting in greater salt build up (Nestler 1977).

Nadir Regression Modeling of *S. alterniflora* AGB:

Of the VIs used in this study, those that utilized red, NIR, and red-edge slope features provided the highest performance for regression models at nadir. RENDVI (Gitelson & Merzlyak 1994, Sims & Gamon 2002) and VREI1 (Vogelmann et al. 1993) both leverage narrowband red-edge reflectance features in the 720-750 nm range, and yielded the most accurate models at the Mature and Young marsh sites, and for both sites combined (Table 7). With the presence of water and sediment background resulting in typical vegetation features being less pronounced in the visible region in the nadir reflectance spectra - while the red-edge remains apparent (Figure 6) - it is understandable that these red-edge indices would provide accurate estimates of AGB.

Additionally, NDVI, MSR, and a number of indices similar in form to NDVI, including IPVI, WDRVI, and TDVI, also yielded strong results for both individual and combined site models (Table 7). These indices all focus on mathematically transforming the sizable differences in red and NIR reflectance typically seen in vegetation canopies, caused by chlorophyll's strong absorption features contrasting with high NIR scattering due to plant cell and canopy structure

(Bannari et al. 1996). With all of these indices leveraging the same spectral features in slightly different ways, their similarly strong performance is expected, with the large difference in red and NIR reflectance being one of the most pronounced features in the nadir plot spectra (Figure 6).

Across the combined and individual site models, the 3 cm nadir imagery yielded the highest performing AGB models in terms of R^2 and NRMSE (Table 7). This was especially evident at the Mature Marsh, where the most accurate 3 cm model had an R^2 of 0.86. The accuracy of models at this site exceeds those found by other studies using lower GSD hyperspectral imagery to model *S. alterniflora* AGB: Wang et al. (2017) and O'Donnell et al. (2016) both found models with R^2 values of 0.70 using multiple and single linear regression, respectively. However, the most accurate 3 cm AGB model for the Young Marsh had an R^2 value of 0.64, demonstrating a sizable decrease in model performance compared to the Mature Marsh and these previous studies. Only small decreases in accuracy were observed between the best 3 cm and 6 cm regression models for individual and combined site models (Table 5, Table 6), suggesting that despite the decrease in GSD, the majority of variability in *S. alterniflora* AGB is still able to be captured and modeled effectively.

The relatively poor model performance at the Young Marsh may be in part due to the greater variance observed in *S. alterniflora* culm heights observed at this site, relative to the Mature Marsh. With *S. alterniflora* height strongly informing AGB (Equations 1 & 2), this additional variability in culm height may be difficult to resolve in these nadir AGB models, given that minimal surface area of these erectophiles are visible when viewed from above. This is supported by the results of the residual analysis performed in this study, which found that nine of the ten models tested had residuals positively correlated with average *S. alterniflora* culm height, indicating that these models were underestimating AGB at plots with short culms, and overestimating AGB when average culm height was high. While the majority of models tested also had residuals positively correlated with *S. alterniflora* culm density, variability in culm density was not significantly different between the Mature and Young Marshes. Additionally, model performance was dramatically higher at the Mature Marsh, despite variability in *S. alterniflora* AGB being significantly higher at this site at a 90% confidence level. Considering these together, regression models were able to accurately encompass a wider range of AGB values at the Mature Marsh than at the Young Marsh, and with culm density averages and variance being similar between sites, suggests that higher variability in culm height at the Young Marsh results in lower accuracy models.

Additionally, for all of the Mature Marsh models, elevation was a significant, negatively correlated predictor of model residuals. With most ground-truth plots at the Mature Marsh being near or beneath mean sea level, this term in the multiple regression model would result in a positive value for these plots, with the value decreasing nearing mean sea level. Since tall-form *S. alterniflora* grows at lower elevations, this correlation is likely overlapping with and amplifying the correlation seen between *S. alterniflora* culm height and model residuals. Alternatively, this may reflect variability in model performance related to differing levels of sediment saturation, which likely decreases as elevation increases. Finally, the 3 cm VREI1 model at the Mature Marsh had residuals positively correlated with benthic chlorophyll *a* concentrations. While not consistently seen in this analysis, and only accounting for approximately 2% of the variance observed in the model residuals, these results suggest that algae may have the potential to interfere with AGB estimates. The presence of algal communities may be decreasing the red reflectance of the sediment surface, increasing the slope of the red-edge that the VREI1 index utilizes, resulting in higher index values. Similarly, algal chlorophyll may affect other VIs by increasing green reflectance and reducing red reflectance of the sediment visible between *S. alterniflora* culms, two spectral features utilized by a large number of VIs. In doing so, algal communities may alter VI values where present, resulting in an overestimate of AGB when using indices sensitive to chlorophyll's spectral features.

Oblique Regression Modeling of *S. alterniflora* AGB:

DVI, MTVI2, TGI, GRVI, MSR, and SR at the 6 m camera elevation yielded the strongest models of AGB based on oblique imaging of the Mature and Young Marshes. DVI, MSR, and SR all utilize the same red and NIR reflectance features that some of the best performing indices at the nadir viewing angle used, however, only MSR was among the top performers at both nadir and oblique viewing angles. Differing from the other indices that performed well in this study, MTVI2 and GRVI incorporate green wavelengths in addition to NIR and/or red wavelengths, while TGI only uses visible blue, green, and red wavelengths. The relatively increased performance of models utilizing green and blue wavelengths at oblique viewing angles may be due to the ability of these angles to better capture the spectral features of *S. alterniflora* in the visible wavelengths (Figure 6, Figure 7). These findings are similar to those of Goldsmith et al. (2020), where among other indices, the Green-Red Vegetation Index (Motohka et al. 2010) was a significant predictor of foliar %N in obliquely angled imagery. While many of the top performing indices at oblique angles leverage the difference between red and NIR reflectance, none of them used red-edge features - which were commonly used among indices providing strong models at nadir views. It may be that red-edge slopes are exaggerated at oblique views, given the difference observed in red-edge slopes between the nadir (Figure 6) and oblique plot-level spectra (Figure 7).

With previous studies finding stronger relationships between canopy characteristics and VIs at off-nadir angles (Chen et al. 2018, Stagakis et al. 2018), I expected that oblique viewing geometries would provide more accurate *S. alterniflora* AGB regression models than nadir views, as more surface area of their narrow, vertically oriented culms would be visible. However, this was not observed, and except for a few cases, AGB models produced from oblique imagery were outperformed by either or both nadir resolution models using the same VI, for all camera elevations/viewing angles tested. Additionally, the exceptions where oblique AGB models provided similar or better accuracy to nadir models represented cases where the VI used performed poorly for the nadir imagery, for example, 6 m TGI at the Mature Marsh, or 6 m DVI at the Young Marsh. In these cases, while the oblique models demonstrated higher R^2 values than their nadir counterparts for that specific VI, their performance comparatively was still far lower than the highest performing nadir models at the site.

Clear trends were observed in the accuracy of oblique AGB models in relation to camera elevation and viewing angle. Across both sites and the combined site models, the 6 m camera elevation - providing the highest viewing angle - typically yielded the highest R^2 and lowest NRMSE models. For the combined site and Mature Marsh models, few regression models for the 2 m camera elevation - representing the shallowest viewing angle collected - were significant. Those that were had extremely low R^2 values (max = 0.15).

For oblique models at the Young Marsh, where an intermediate, 4 m camera elevation was available for analysis, average model performance across all indices decreased consistently going from high to low viewing angles, further supporting the trends seen in the Mature Marsh and combined models. While a small number of indices at 4 m provided comparable or better performance than the 6 m equivalent (GOSAVI, MCARI2, OSAVI), the 4 m models outperformed the 2 m models in every case. Interestingly, the three indices that saw slight improvements from 6 m to 4 m mast elevations all incorporate a soil adjustment factor into the index equation. With these soil adjustment factors remaining constant between all oblique and nadir views at the default values shown in Table 1, it may be that the amount of background sediment visible was best represented by these adjustment factors at the viewing angle provided by the 4 m oblique imagery.

These findings suggest that shallow viewing angles are not suitable for AGB regression modeling using VIs in salt marsh ecosystems, and that the steeper viewing angles provided by higher camera elevations provide more accurate regression models of *S. alterniflora* AGB. However, assessing AGB using nadir views will most likely provide the strongest regression models. Counterintuitively, this may be caused by more sediment background being visible in between *S. alterniflora* culms from nadir/higher viewing angles, reducing VI values in plots with low culm densities more than in plots with high densities - allowing for culm density to be reflected in plot-level average VI values. However, oblique viewing geometries result in more sediment background being obscured by culms, which can be seen by comparing the reflectance spectra in Figure 6 and Figure 7. Typically, oblique views yielded plot-level reflectance spectra with higher green and NIR reflectance, steeper red-edge slopes, and more prominent red absorption features than the same plots viewed from nadir. Additionally, these features became increasingly pronounced at both sites as viewing angle decreased with lower camera elevations (Figure 7). While these oblique views capture the reflectance features of *S. alterniflora* well, it may also make it more challenging to estimate AGB using regression modeling methods. Finally, oblique viewing angles present opportunities for culms closer to the sensor to occlude those behind them, which may result in the loss of valuable spectral information, or introduce error into models if culms in the foreground are overlapping with - or are indistinguishable from - those within a plot.

***S. alterniflora* Regression Modeling Considerations:**

These results find that while the most accurate models were obtained using 3 cm nadir drone data, there is roughly comparable average performance between 3 cm and 6 cm nadir drone resolutions. With minimal changes in reflectance and NDVI values being observed between UAS flights within our operating elevations (Stow et al. 2019), this is not entirely unexpected. Furthermore, Fawcett et al. (2020) found strong agreement in maize NDVI and CHL indices for GSD values ranging from 4.15 cm to 20 m, demonstrating a level of consistency in observations between scales for the remote sensing of vegetation.

This suggests that if a large extent of salt marsh requires evaluation, the 6 cm spatial resolution would allow complete coverage in less time, while maintaining most of the accuracy. However, if accurate AGB estimates are paramount, the study area small, or time not a consideration, higher spatial resolutions will still provide the most accurate estimates of AGB. How much the spatial resolution can be lowered while maintaining approximately equivalent accuracy to higher resolutions is unknown and beyond the scope of this study, and there is likely a limit where losses in accuracy become noticeable at GSD becomes larger. This can be seen in the regression models found by O'Donnell et al. (2016), which found that while scaling from 1 m hyperspectral to 30 m Landsat imagery, the best regression model at 1 m GSD had an R^2 of 0.70, compared to an R^2 of 0.51 for the 30 m GSD landsat imagery.

Additionally, comparing between viewing angles suggests that regression modeling of *S. alterniflora* AGB is unlikely to be successful using obliquely angled imagery, given the overall poor accuracy seen across all indices and viewing angles tested at both marsh sites. However, using oblique imagery in conjunction with an inversion of the PROSAIL radiative transfer model has been shown to yield accurate retrievals of AGB across the same salt marsh chronosequence sites used in this study (Eon et al. 2019). While the highest performing combined site oblique regression model of AGB in this study had an R^2 of 0.33, the PROSAIL inversion performed by Eon et al. (2019) had an R^2 of 0.73 for observed vs. predicted AGB values across the same Mature and Young Marshes studied here - which additionally outperforms the highest R^2 nadir regression model found in this study (R^2 - 0.65).

Finally, plot-level spectra collected as part of this study illustrate some of the challenges of remote sensing within salt marsh ecosystems. While general consistency is observed between 3 cm and 6 cm nadir spectra at the Mature Marsh, sizable differences are apparent between the two sets of spectra collected at the Young Marsh (Figure 6). The 3 cm flight at the Young Marsh almost overlapped with low tide, while the 6 cm flight took place approximately an hour prior, closer to the high tide occurring roughly six hours before. Despite this small difference in timing, major differences are observed in the spectra collected between these two flights. The 6 cm spectra have reduced reflectance overall compared to the 3 cm spectra, which is especially apparent in the NIR region - resulting in lower red-edge slopes in the 6 cm spectra. This is likely due to the larger sand fraction (Goldsmith 2019) and lower SOM (Table 2) found at the Young Marsh, leading to it being more well-drained than the Mature Marsh. Because less water is retained in the sediment over time, and can likely infiltrate and percolate through the sediment faster, spectra and VIs collected from the Young Marsh seem to be more sensitive to tidal changes. This is supported by the results of the residual analysis, where models at the Young Marsh often had residuals correlated with BD at a 1 cm depth - indicating model performance was impacted by variation in surface sediment characteristics that not only affect the reflectance of the sediment itself, but also its water retention. This contrasts with observations at the Mature Marsh. While the amount of time between 3 cm and 6 cm flights was shorter at the Mature Marsh, the consistency in spectral characteristics between flights may also be in part due to the SOM (Table 2) and clay rich sediment (Goldsmith 2019) found at the site, which may retain water and stay saturated more consistently, thus retaining the same spectral features despite changing tides.

Evaluation of Interseasonal Model Applicability:

Of the five best performing models from the 6 m camera elevation and viewing angle, providing the highest performance in July 2019, interseasonal model performance was typically poor. For the MSR, RENDVI, TDVI, and SR models of AGB, RMSE and NRMSE between observed and predicted AGB values were higher when applying the model to the same plots in the October imagery, when compared to July 2019. For these four models, the AGB values predicted in October did not follow the expected 1:1 line, with the majority of these predictions being underestimates of AGB (Figure 9). Given the senescence occurring by October, with plants turning a yellow-brown hue due to increased red reflectance, and reduced NIR reflectance and red-edge slopes being observed (Figure 8), it is understandable that model performance would decrease between months. These models likely yield poor results because they cannot account for these changes in phenology that have occurred between seasons, as the data used to train the model was obtained from July only.

Interestingly, the GRVI model of AGB actually had lower RMSE and NRMSE when applied to the October imagery than when applied in the original month, which demonstrates that this model retains a level of accuracy when predicting AGB across months, despite changes in plant phenology over time. Additionally, observed vs. predicted values followed the 1:1 line, with no major deviations or trends being observed. This model may be more suited to interseasonal application because it divides NIR reflectance by green reflectance. Since green reflectance remained similar between July and October, and only small decreases in NIR reflectance were observed (Figure 8), the resulting values from the GRVI index were similar between months at the same plots (Figure 10). Although low values of GRVI in July become higher in October, and high values become lower, they still roughly follow the 1:1 line.

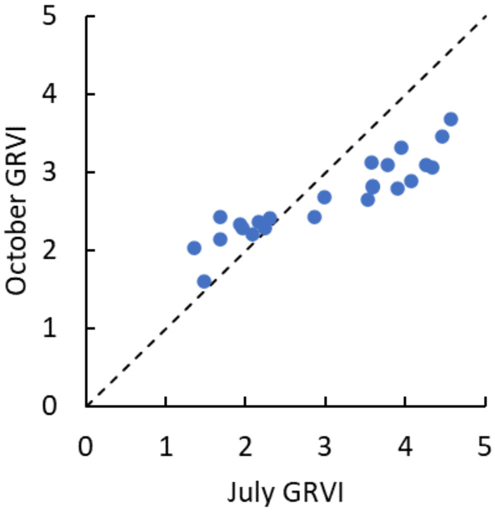

Figure 10: Comparison of GRVI values in July and October 2019, for the subset of plots resampled in October 2019.

Conclusions and Future Work:

When available or practical to collect, using the highest GSD nadir imagery possible will likely maximize the accuracy of AGB regression models in *S. alterniflora* dominated salt marshes. However, these results indicate that only minimal model accuracy is lost going from 3 cm to 6 cm GSD, indicating that slightly lower resolutions can still produce accurate AGB estimates. This is an important consideration when selecting parameters for UAS data collection: a slight decrease in model accuracy can allow for the evaluation of a larger area in the same amount of time. Depending on the application, this trade-off may be worthwhile. Additionally, nadir imagery vastly outperforms obliquely angled imagery for AGB assessment when using regression modeling techniques. However, obliquely angled imaging is still powerful for evaluating salt marsh health (Goldsmith et al. 2020), or for retrieving AGB using an inverted radiative transfer model, such as PROSAIL (Eon et al. 2019).

Between the two marsh sites, various VIs leveraging NIR reflectance and red-edge slope performed well. The two visible band indices used by this study (TGI & TVI) yielded poor AGB estimates, suggesting that visible bands alone are not sufficient to provide accurate estimates of AGB. For the best performing nadir models, residuals consistently positively correlated with *S. alterniflora* height - AGB was often underestimated when culm height was short, and overestimated when culms were taller. This may be due to the erectophile canopy structure of *S. alterniflora*, where height is likely challenging to observe from nadir views. With this understanding, augmenting hyperspectral analyses with LIDAR data may provide important information regarding canopy height, which could further improve AGB models and estimates.

Finally, interseasonal model applicability likely depends on the specific index used. While four models using NIR, red, and red-edge wavelengths yielded poor results between seasons, the one model using NIR and green wavelengths demonstrated similar accuracy from July to October, indicating that interseasonal application of GRVI may yield acceptably accurate AGB estimates despite seasonal differences in plant phenology.

This study is a first step towards understanding the differences in AGB estimates produced across platforms with varying GSDs and viewing angles. Additional work should be performed to identify if spectral smoothing techniques, such as Savistsky-Golay filters, can improve VI model results compared to the original spectra. Additionally, future work should perform sensitivity analysis on broadband vegetation indices to identify which combinations of spectral bands yield the strongest AGB models and estimates, rather than using just the central wavelength for the broadband region. By performing this analysis across a large number of vegetation indices leveraging visible and NIR features, it should be possible to identify any wavelengths that are consistently strong at predicting AGB within *S. alterniflora* communities.

Future work should also include testing the interseasonal application of a wider array of VIs using nadir imagery, to evaluate model accuracy between seasons using the most accurate viewing angle available, and should test the interseasonal performance of AGB retrievals from inverted radiative transfer models, such as PROSAIL. Additionally, comparing AGB estimates from regression models to AGB retrievals produced by inverted radiative transfer models may also yield important insight into their respective accuracies at various viewing angles and GSDs. Finally, future work should expand this analysis to include imagery collected from lower GSD airborne and satellite platforms, to evaluate how the accuracy of AGB estimates continue to change with spatial resolution.

Taken together, these results demonstrate the ability for remote sensing to provide us with valuable and accurate information regarding salt marsh AGB, and in turn, carbon storage. However, these results also illustrate some of the challenges associated with evaluating the heterogeneity present within these dynamic tidal ecosystems, and reveal differences in the accuracy of regression models of *S. alterniflora* AGB between GSDs, viewing angles, seasons, and across marshes of varying ages that highlight the need for careful selection and application of remote sensing techniques to yield the strongest results. Future research and investigations into salt marsh AGB using regression modeling should consider these findings when selecting what GSD and viewing angle to collect imagery from, to maximize model accuracy and improve evaluations of salt marsh carbon storage. In doing so, land managers can direct restoration efforts towards areas affected by stressors, and conservation towards the most productive salt marshes.

Works Cited:

AL3 Lift Series. (n.d.). Retrieved March 9, 2020, from https://blueskymast.com/mast-systems/al3-lift-series/

Armstrong, R. A. (1993). Remote sensing of submerged vegetation canopies for biomass estimation. International Journal of Remote Sensing, 14(3), 621–627. https://doi.org/10.1080/01431169308904363

Aspila, K. I., Agemian, H., & Chau, A. S. Y. (1976). A semi-automated method for the determination of inorganic, organic and total phosphate in sediments. The Analyst, 101(1200), 187. doi: 10.1039/an9760100187

Bachmann, C. M., Eon, R. S., Lapszynski, C. S., Badura, G. P., Vodacek, A., Hoffman, M. J., … Foote, M. (2019). A Low-Rate Video Approach to Hyperspectral Imaging of Dynamic Scenes. Journal of Imaging , Vol. 5. https://doi.org/10.3390/jimaging5010006

Bannari, A., Morin, D., Bonn, F., & Huete, A. (1996). A review of vegetation indices. Remote Sensing Reviews, 13, 95–120. https://doi.org/10.1080/02757259509532298

Bannari, A., Asalhi, H., & Teillet, P. M. (2002). Transformed difference vegetation index (TDVI) for vegetation cover mapping. IEEE International Geoscience and Remote Sensing Symposium, 5, 3053–3055 vol.5. https://doi.org/10.1109/IGARSS.2002.1026867

Berg, P., & McGlathery, K. J. (2001). A high-resolution pore water sampler for sandy sediments. Limnology and Oceanography, 46(1), 203–210. https://doi.org/10.4319/lo.2001.46.1.0203

Bertness, M. D., Ewanchuk, P. J., & Silliman, B. R. (2002). Anthropogenic modification of New England salt marsh landscapes. Proceedings of the National Academy of Sciences of the United States of America, 99(3), 1395–1398. https://doi.org/10.1073/pnas.022447299

Bridgham, S. D., Megonigal, J. P., Keller, J. K., Bliss, N. B., & Trettin, C. (2006). The carbon balance of North American wetlands. Wetlands, 26(4), 889–916. https://doi.org/10.1672/0277-5212(2006)26[889:TCBONA]2.0.CO;2bac

Broge, N. H., & Leblanc, E. (2001). Comparing prediction power and stability of broadband and hyperspectral vegetation indices for estimation of green leaf area index and canopy chlorophyll density. Remote Sensing of Environment, 76(2), 156–172. https://doi.org/https://doi.org/10.1016/S0034-4257(00)00197-8

Chastain, S. G., Kohfeld, K., & Pellatt, M. G. (2018). Carbon Stocks and Accumulation Rates in Salt Marshes of the Pacific Coast of Canada. Biogeosciences Discussions, (April), 1–45. https://doi.org/10.5194/bg-2018-166

Chen, J. M. (1996). Evaluation of Vegetation Indices and a Modified Simple Ratio for Boreal Applications. Canadian Journal of Remote Sensing, 22(3), 229–242. https://doi.org/10.1080/07038992.1996.10855178

Chen, H., Huang, W., Li, W., Niu, Z., Zhang, L., & Xing, S. (2018). Estimation of LAI in Winter Wheat from Multi-Angular Hyperspectral VNIR Data: Effects of View Angles and Plant Architecture. Remote Sensing, 10(10). https://doi.org/10.3390/rs10101630

Christiansen, T., Wiberg, P. L., & Milligan, T. G. (2000). Flow and Sediment Transport on a Tidal Salt Marsh Surface. Estuarine, Coastal and Shelf Science, 50(3), 315–331. https://doi.org/https://doi.org/10.1006/ecss.2000.0548

Costanza, R., D'Arge, R., de Groot, R., Farber, S., Grasso, M., Hannon, B., … van den Belt, M. (1997). The value of the world's ecosystem services and natural capital. Nature, 387(May), 253–260. Retrieved from https://www.nature.com/articles/387253a0.pdf

Costanza, R., de Groot, R., Sutton, P., van der Ploeg, S., Anderson, S. J., Kubiszewski, I., … Turner, R. K. (2014). Changes in the global value of ecosystem services. Global Environmental Change, 26(1), 152–158. https://doi.org/10.1016/j.gloenvcha.2014.04.002

Crippen, R. E. (1990). Calculating the vegetation index faster. Remote Sensing of Environment, 34(1), 71–73. https://doi.org/https://doi.org/10.1016/0034-4257(90)90085-Z

Deaton, C. D., Hein, C. J., & Kirwan, M. L. (2017). Barrier island migration dominates ecogeomorphic feedbacks and drives salt marsh loss along the Virginia Atlantic Coast, USA. Geology. https://doi.org/10.1130/G38459.1

Donnelly, J. P., & Bertness, M. D. (2001). Rapid shoreward encroachment of salt marsh cordgrass in response to accelerated sea-level rise. Proceedings of the National Academy of Sciences of the United States of America, 98(25), 14218–14223. https://doi.org/10.1073/pnas.251209298

Doughty, C. L., & Cavanaugh, K. C. (2019). Mapping coastal wetland biomass from high resolution unmanned aerial vehicle (UAV) imagery. Remote Sensing, 11(5). https://doi.org/10.3390/rs11050540

Duarte, C. M., Middelburg, J. J., & Caraco, N. (2005). Major role of marine vegetation on the oceanic carbon cycle. Biogeosciences, 2(1), 1–8. https://doi.org/10.5194/bg-2-1-2005

Ellison, A. M., Bertness, M. D., & Miller, T. (1986). Seasonal Patterns in the Belowground Biomass of *Spartina alterniflora* (Gramineae) Across a Tidal Gradient. American Journal of Botany, 73(11), 1548–1554. https://doi.org/https://doi.org/10.1002/j.1537-2197.1986.tb10905.x

Eon, R. S., Goldsmith, S., Bachmann, C. M., Tyler, A. C., Lapszynski, C. S., Badura, G. P., … Brett, R. (2019). Retrieval of salt marsh above-ground biomass from high-spatial resolution hyperspectral imagery using PROSAIL. Remote Sensing, 11(11), 1–18. https://doi.org/10.3390/rs11111385

Fawcett, D., Panigada, C., Tagliabue, G., Boschetti, M., Celesti, M., Evdokimov, A., … Anderson, K. (2020). Multi-Scale Evaluation of Drone-Based Multispectral Surface Reflectance and Vegetation Indices in Operational Conditions. Remote Sensing, 12(3). https://doi.org/10.3390/rs12030514

Foley, W. J., McIlwee, A., Lawler, I., Aragones, L., Woolnough, A. P., & Berding, N. (1998). Ecological applications of near infrared reflectance spectroscopy – a tool for rapid, cost-effective prediction of the composition of plant and animal tissues and aspects of animal performance. Oecologia, 116(3), 293–305. https://doi.org/10.1007/s004420050591

Gedan, K. B., Silliman, B. R., & Bertness, M. D. (2009). Centuries of Human-Driven Change in Salt Marsh Ecosystems. Annual Review of Marine Science, 1(1), 117–141. https://doi.org/10.1146/annurev.marine.010908.163930

General Dynamics Vector 20 Maritime Pan Tilt. Available online: https://www.gd-ots.com/wp-content/uploads/2017/11/Vector-20-Stabilized-Maritime-Pan-Tilt-System-1.pdf

Gitelson, A., & Merzlyak, M. N. (1994). Spectral Reflectance Changes Associated with Autumn Senescence of *Aesculus hippocastanum* L. and *Acer platanoides* L. Leaves. Spectral Features and Relation to Chlorophyll Estimation. Journal of Plant Physiology, 143(3), 286–292. https://doi.org/10.1016/S0176-1617(11)81633-0

Gitelson, A. A., & Merzlyak, M. N. (1998). Remote sensing of chlorophyll concentration in higher plant leaves. Advances in Space Research, 22(5), 689–692. https://doi.org/https://doi.org/10.1016/S0273-1177(97)01133-2

Gitelson, A. A. (2004). Wide Dynamic Range Vegetation Index for Remote Quantification of Biophysical Characteristics of Vegetation. Journal of Plant Physiology, 161(2), 165–173. https://doi.org/https://doi.org/10.1078/0176-1617-01176

Goel, N. S., & Qin, W. (1994). Influences of canopy architecture on relationships between various vegetation indices and LAI and Fpar: A computer simulation. Remote Sensing Reviews, 10(4), 309–347. https://doi.org/10.1080/02757259409532252

Goldsmith, S. B. (2019). Decadal Changes in Salt Marsh Succession and Assessing Salt Marsh Vulnerability using High-Resolution Hyperspectral Imagery. (Master's thesis). Retrieved from https://scholarworks.rit.edu/theses/10381

Goldsmith, S. B., Eon, R. S., Lapszynski, C. S., Badura, G. P., Osgood, D. T., Bachmann, C. M., & Tyler, A. C. (2020). Assessing Salt Marsh Vulnerability Using High-Resolution Hyperspectral Imagery. 1–21. https://doi.org/10.3390/rs12182938

Haboudane, D., Miller, J. R., Pattey, E., Zarco-Tejada, P. J., & Strachan, I. B. (2004). Hyperspectral vegetation indices and novel algorithms for predicting green LAI of crop canopies: Modeling and validation in the context of precision agriculture. Remote Sensing of Environment, 90(3), 337–352. https://doi.org/10.1016/j.rse.2003.12.013

He, Y., Widney, S., Ruan, M., Herbert, E., Li, X., & Craft, C. (2016). Accumulation of soil carbon drives denitrification potential and lab-incubated gas production along a chronosequence of salt marsh development. Estuarine, Coastal and Shelf Science, 172, 72–80. https://doi.org/https://doi.org/10.1016/j.ecss.2016.02.002

Hunt Jr., E. R., Daughtry, C. S. T., Eitel, J. U. H., & Long, D. S. (2011). Remote Sensing Leaf Chlorophyll Content Using a Visible Band Index. Agronomy Journal, 103(4), 1090–1099. https://doi.org/https://doi.org/10.2134/agronj2010.0395

Jeffrey, S. W., & Humphrey, G. F. (1975). New spectrophotometric equations for determining chlorophylls a, b, c1 and c2 in higher plants, algae and natural phytoplankton. Biochemie Und Physiologie Der Pflanzen, 167(2), 191–194. https://doi.org/10.1016/s0015-3796(17)30778-3

Jordan, C. F. (1969). Derivation of Leaf-Area Index from Quality of Light on the Forest Floor. Ecology. https://doi.org/10.2307/1936256

Kearney, M. S., & Grace, R. E. (1988). Marsh loss in Nanticoke estuary, Chesapeake Bay. 78(2).

Kirwan, M. L., Guntenspergen, G. R., & Morris, J. T. (2009). Latitudinal trends in *Spartina alterniflora* productivity and the response of coastal marshes to global change. Global Change Biology, 15(8), 1982–1989. https://doi.org/10.1111/j.1365-2486.2008.01834.x

Martynenko, A., Shotton, K., Astatkie, T., Petrash, G., Fowler, C., Neily, W., & Critchley, A. T. (2016). Thermal imaging of soybean response to drought stress: the effect of

Ascophyllum nodosum seaweed extract. SpringerPlus. https://doi.org/10.1186/s40064-016-3019-2

McLeod, E., Chmura, G. L., Bouillon, S., Salm, R., Björk, M., Duarte, C. M., … Silliman, B. R. (2011). A blueprint for blue carbon: Toward an improved understanding of the role of vegetated coastal habitats in sequestering CO2. Frontiers in Ecology and the Environment, 9(10), 552–560. https://doi.org/10.1890/110004

Mcowen, C. J., Weatherdon, L. V., Van Bochove, J. W., Sullivan, E., Blyth, S., Zockler, C., … Fletcher, S. (2017). A global map of saltmarshes. Biodiversity Data Journal, 5(1). https://doi.org/10.3897/BDJ.5.e11764

McTigue, N., Davis, J., Rodriguez, A., McKee, B., Atencio, A., & Currin, C.. (2020).Dataset: Carbon accumulation rates in a salt marsh over the past two millennia(Version1).Smithsonian Environmental Research Center. https://doi.org/10.25573/serc.11421063.v1

Minchinton, T. E., & Bertness, M. D. (2003). Disturbance-mediated competition and the spread of *Phragmites australis* in a coastal marsh. Ecological Applications. https://doi.org/10.1890/02-5136

Miller, G. J., Morris, J. T., & Wang, C. (2019). Estimating Aboveground Biomass and Its Spatial Distribution in Coastal Wetlands Utilizing Planet Multispectral Imagery. Remote Sensing, 11(17), 2020. https://doi.org/10.3390/rs11172020

Morgan, P. A., & Short, F. T. (2002). Using Functional Trajectories to Track Constructed Salt Marsh Development in the Great Bay Estuary, Maine/New Hampshire, U.S.A.

Restoration Ecology, 10(3), 461–473. https://doi.org/https://doi.org/10.1046/j.1526-100X.2002.01037.x

Motohka, T., Nasahara, K. N., Oguma, H., & Tsuchida, S. (2010). Applicability of Green-Red Vegetation Index for Remote Sensing of Vegetation Phenology. Remote Sensing , Vol. 2, pp. 2369–2387. https://doi.org/10.3390/rs2102369

Murphy, J., & Riley, J. P. (1962). A modified single solution method for the determination of phosphate in natural waters. Analytica Chimica Acta, 27, 31–36. https://doi.org/https://doi.org/10.1016/S0003-2670(00)88444-5

Nestler, J. (1977). Interstitial salinity as a cause of ecophenic variation in *Spartina alterniflora*. Estuarine and Coastal Marine Science, 5, 707–714. https://doi.org/10.1016/0302-3524(77)90043-3

O'Donnell, J. P. R., & Schalles, J. F. (2016). Examination of abiotic drivers and their influence on *Spartina alterniflora* biomass over a twenty-eight year period using Landsat 5 TM satellite imagery of the Central Georgia Coast. Remote Sensing, 8(6). https://doi.org/10.3390/rs8060477

Osgood, D. T., & Zieman, J. C. (1993). Spatial and Temporal Patterns of Substrate Physicochemical Parameters in Different-aged Barrier Island Marshes. Estuarine Coastal and Shelf Science, 37, 421–436. https://doi.org/10.1006/ecss.1993.1065

Pennings, S. C., Grant, M.-B., & Bertness, M. D. (2005). Plant Zonation in Low-Latitude Salt Marshes: Disentangling the Roles of Flooding, Salinity and Competition. Journal of Ecology, 93(1), 159–167. http://www.jstor.org/stable/3599466

Qi, J., Chehbouni, A., Huete, A. R., Kerr, Y. H., & Sorooshian, S. (1994). A modified soil adjusted vegetation index. Remote Sensing of Environment, 48(2), 119–126. https://doi.org/10.1016/0034-4257(94)90134-1

Rendong, L., & Jiyuan, L. (2004). Estimating wetland vegetation biomass in the Poyang Lake of central China from landsat ETM data. International Geoscience and Remote Sensing Symposium (IGARSS), 7(C), 4590–4593. https://doi.org/10.1109/igarss.2004.1370177

Richards, C. L., Pennings, S. C., & Donovan, L. A. (2005). Habitat range and phenotypic variation in salt marsh plants. Plant Ecology, 176(2), 263–273. https://doi.org/10.1007/s11258-004-0841-3

Rondeaux, G., Steven, M., & Baret, F. (1996). Optimization of soil-adjusted vegetation indices. Remote Sensing of Environment, 55(2), 95–107. https://doi.org/https://doi.org/10.1016/0034-4257(95)00186-7

Roujean, J.-L., & Breon, F.-M. (1995). Estimating PAR absorbed by vegetation from bidirectional reflectance measurements. Remote Sensing of Environment, 51(3), 375–384. https://doi.org/https://doi.org/10.1016/0034-4257(94)00114-3

Schalles, J. F., Hladik, C. M., Lynes, A. A., & Pennings, S. C. (2013). Landscape estimates of habitat types, plant biomass, and invertebrate densities in a Georgia salt marsh. Oceanography, 26(3), 88–97. https://doi.org/10.5670/oceanog.2013.50

Sims, D. A., & Gamon, J. A. (2002). Relationships between leaf pigment content and spectral reflectance across a wide range of species, leaf structures and developmental stages. Remote Sensing of Environment, 81(2), 337–354. https://doi.org/https://doi.org/10.1016/S0034-4257(02)00010-X

Sripada, R., et al. (2005). Determining In-Season Nitrogen Requirements for Corn Using Aerial Color-Infrared Photography. (Ph.D. dissertation, North Carolina State University). Retrieved from https://repository.lib.ncsu.edu/handle/1840.16/4200

Sripada, R. P., Heiniger, R. W., White, J. G., & Meijer, A. D. (2006). Aerial Color Infrared Photography for Determining Early In-Season Nitrogen Requirements in Corn. Agronomy Journal, 98(4), 968–977. https://doi.org/https://doi.org/10.2134/agronj2005.0200

Stagakis, S., Markos, N., Sykioti, O., & Kyparissis, A. (2010). Monitoring canopy biophysical and biochemical parameters in ecosystem scale using satellite hyperspectral imagery: An application on a *Phlomis fruticosa* Mediterranean ecosystem using multiangular CHRIS/PROBA observations. Remote Sensing of Environment, 114, 977–994. https://doi.org/10.1016/j.rse.2009.12.006

Stow, D., Nichol, C. J., Wade, T., Assmann, J. J., Simpson, G., & Helfter, C. (2019). Illumination Geometry and Flying Height Influence Surface Reflectance and NDVI Derived from Multispectral UAS Imagery. Drones, 3(3). https://doi.org/10.3390/drones3030055

Stumpf, R. P. (1983). The process of sedimentation on the surface of a salt marsh. Estuarine, Coastal and Shelf Science, 17(5), 495–508. https://doi.org/https://doi.org/10.1016/0272-7714(83)90002-1

Tiner, R.W., J.Q. Swords, and B.J. McClain. (2002). Wetland Status and Trends for the Hackensack Meadowlands. An Assessment Report from the U.S. Fish and Wildlife Service's National Wetlands Inventory Program. U.S. Fish and Wildlife Service, Northeast Region, Hadley, MA. 29 pp.

Trimble R10: Integrated GNSS Systems: Trimble Geospatial. (n.d.). Retrieved April 10, 2020, from https://geospatial.trimble.com/products-and-solutions/r10

Tyler, A. C., & Joseph C Zieman. (1999). Patterns of development in the creekbank region of a barrier island *Spartina alterniflora* marsh . Marine Ecology Progress Series, 180, 161–177. Retrieved from https://www.int-res.com/abstracts/meps/v180/p161-177/

Tyler, A. C., Mastronicola, T. A., & McGlathery, K. J. (2003). Nitrogen fixation and nitrogen limitation of primary production along a natural marsh chronosequence. Oecologia, 136(3), 431–438. https://doi.org/10.1007/s00442-003-1277-5

Valiela, I., Teal, J. M., & Deuser, W. G. (1978). The Nature of Growth Forms in the Salt Marsh Grass *Spartina alterniflora*. The American Naturalist, 112(985), 461–470. https://doi.org/10.1086/283290

Vogelmann, J. E., Rock, B. N., & Moss, D. M. (1993). Red edge spectral measurements from sugar maple leaves. International Journal of Remote Sensing, 14(8), 1563–1575. https://doi.org/10.1080/01431169308953986

Walsh, J. P. (1998). Low marsh succession along an over-wash salt marsh chronosequence (University of Virginia PP - United States -- Virginia). Retrieved from https://ezproxy.rit.edu/login?url=https://www.proquest.com/dissertations-theses/low-marsh-succession-along-over-wash-salt/docview/304459319/se-2?accountid=108

Wang, J., Liu, Z., Yu, H., & Li, F. (2017). Mapping *Spartina alterniflora* biomass using LiDAR and hyperspectral data. Remote Sensing, 9(6), 1–14. https://doi.org/10.3390/rs9060589

Yang, Z., Willis, P., & Mueller, R. (2008). Impact of Band-Ratio Enhanced AWIFS Image on Crop Classification Accuracy.